Research Article

Dynamic Response of Graphitic Targets with Tantalum Cores Impacted by Pulsed 440-GeV Proton Beams

Pascal Simon [1,2] **Philipp Drechsel** [1,2] **Peter Katrik** [2] **Kay-Obbe Voss** [2] **Philipp Bolz** [1,2] **Fiona J. Harden** [3] **Michael Guinchard** [3] **Yacine Kadi** [3] **Christina Trautmann** [1,2] **and Marilena Tomut** [1,4]

[1]*Materials Research Department, GSI Helmholtzzentrum, Darmstadt 64291, Germany*
[2]*Department of Materials and Earth Sciences, Technische Universität Darmstadt, Darmstadt 64287, Germany*
[3]*CERN, Geneva 1211, Switzerland*
[4]*Institute of Materials Physics, WWU Münster, Münster 48149, Germany*

Correspondence should be addressed to Marilena Tomut; mtomut@uni-muenster.de

Various graphite targets with a tantalum core were exposed to 440 GeV pulsed proton beams at the HiRadMat facility at CERN. The dynamic response was investigated by monitoring the surface velocity of the samples by laser Doppler vibrometry. The study comprises different graphite grades, such as polycrystalline, expanded and carbon-fiber reinforced graphite, and low-density graphitic foams, all candidates for beam-intercepting devices in high-power accelerators. The purpose of the tantalum core is to concentrate the large energy deposition in this high-density material that withstands the localized beam-induced temperature spike. The generated pressure waves are estimated to result in stresses of several hundred MPa which subsequently couple with the surrounding graphite materials where they are damped. Spatial energy deposition profiles were obtained by the Monte Carlo code FLUKA and the dynamic response was modelled using the implicit code ANSYS. Using advanced post-processing techniques, such as fast Fourier transformation and continuous wavelet transformation, different pressure wave components are identified and their contribution to the overall dynamic response of a two-body target and their failure mode are discussed. We show that selected low-intensity beam impacts can be simulated using straight-forward transient coupled thermal/structural implicit simulations. Carbon-fiber reinforced graphites exhibit large (macroscopic) mechanical strength, while their low-strength graphite matrix is identified as a potential source of failure. The dynamic response of low-density graphitic foams is surprisingly favourable, indicating promising properties for the application as high-power beam dump material.

1. Introduction

Beam-intercepting devices (BIDs) such as collimators, beam dumps, beam windows, or production targets are accelerator components that must withstand the interaction with charged particle beams by design. Operation in the high-dose environment of high-power accelerators is characterized by long-term accumulation of radiation damage during the lifetime of the component and dynamic effects due to repetitive transient energy depositions.

Many BIDs of current accelerators such as the Large Hadron Collider (LHC) at CERN [1] or the future Facility for Antiproton and Ion Research (FAIR) [2] are made of various graphitic materials. Depending on their specific area of application, isotropic polycrystalline graphites (PGs), carbon-fiber-reinforced graphites (CFCs), or low-density expanded graphites (EGs) are used. In general, graphite has several advantageous material properties like low atomic number ($Z = 6$) and density ($\rho = 0.5$–$2.2 \, \mathrm{g \cdot cm^{-3}}$) that lead to low radioactivation by relativistic particle beams and low specific energy deposition by interacting beams. The high thermal (up to hundreds of W/mK) [3] and electrical conductivity [4, 5], large service temperature in vacuum conditions (up to 3000 K) [6], high specific strength, and

large radiation-hardness make graphite a widely used material in high-dose environments such as fusion, fission, and accelerator applications [7, 8].

With the continuous effort to increase the beam energy and intensity of high-power accelerators together with decreasing pulse lengths, BIDs have to cope with larger dynamic beam-induced mechanical loads due to repetitive, fast transient energy-deposition events (several kJ·cm^{-3}) that heat small, spatially constrained volumes inside the component by hundreds of Kelvin within few microseconds [9]. These dynamic loads can lead to short-term failure of BIDs even in the absence of long-term radiation damage [3, 10].

In literature, mechanical properties like tensile strength or maximum allowable strain under dynamic loads are reported only for a small fraction of graphitic materials. Furthermore, the large variations in density, the sensitivity to micro- and mesostructure, and the brittleness of graphite make numerical simulations unreliable for the identification of failure limits. In this context, irradiation experiments were already conducted to assess the performance of implicit and explicit numerical models with respect to prototype BIDs [11, 12]. But, catastrophic failure of graphite materials by beam-induced dynamic mechanical loads has yet to be observed. This is mainly due to the very low specific energy deposition in graphite (in comparison to metals, for example) and limitations in the beam intensity at current facilities.

This article reports first results of the HRMT-38 "FlexMat" experiment in which various graphite materials of cylindrical geometry (typically 10 mm in length and in diameter) were impacted by a focussed high-intensity and short-pulse proton beam of 440 GeV/c momentum at the High-Radiation to Materials (HiRadMat) facility at the Super Proton Synchrotron of CERN [13, 14]. Ten targets contained a press-fit tantalum "core" of 3 mm diameter. The specific energy deposition per primary particle is up to 13 times larger in tantalum ($Z = 73$, $\rho = 16.6$ g·cm^{-3}) than in graphite. The ~10 times larger Young's modulus of tantalum ($E_{Ta} = 165$ GPa, $E_{PG} = 11.5$ GPa) leads to beam-induced transient stress waves with amplitudes in the order of hundred MPa for a low-intensity pulse of ~10^{11} protons (transversal beam sigma 1.5 mm). By coupling of the stress waves into the surrounding graphite, much higher dynamic loads can be achieved than in the case of direct beam impact on graphite. By progressively increasing the beam intensity per pulse, possible failure was induced in the different graphite samples. For this, the dynamic response of the targets was monitored using laser Doppler vibrometry and analysed with data analysis techniques such as fast Fourier transformation (FFT) and continuous wavelet transformation (CWT).

At low beam intensities, where the target response is still elastic, the dynamic response was modelled using the implicit code ANSYS. Spatial energy deposition profiles were obtained by employing the Monte Carlo code FLUKA [15], which simulates the interaction and transport of the primary beam within the targets, while taking the transverse beam profile and beam eccentricity observed during the experiment into account. These energy deposition maps served as input for transient thermal simulations. The dynamic mechanical response based

on the beam-induced temperature profile was evaluated in a subsequent coupled transient structural simulation.

2. Materials and Methods

2.1. Experimental Layout and Online Monitoring Instrumentation. The experimental setup comprised six individual target stations, each with a total length of 144 mm mounted on a vertical displacement stage (Figure 1). Each target station accommodated a series of up to 10 cylindrical samples with a diameter and length of 10 mm. The target station could be driven into a fixed irradiation position by a remote-controlled vertical translation stage. The target station and stage were mounted inside a stainless-steel chamber. The proton beam was coupled into and out of the chamber through beam windows made of glassy carbon/ carbon-fiber reinforced graphite sandwich [16]. For safety purposes, the irradiation of the samples was conducted in an argon underpressure atmosphere ($\leq 10^{-2}$ mbar). In the event of a vacuum leak, atmosphere would flow into the chamber preventing the potential spread of radioactive debris from inside the chamber. In case the target station would heat up considerably, the temperature of the target station could be regulated by remotely replenishing the argon atmosphere in the chamber.

Online monitoring equipment included multiple PT100 thermocouples per target station and HBM XY9 bi-directional strain gauges on each sample (48 in total) [17] in order to record the beam-induced axial and tangential strain. A so-called beam television system (BTV) consisting of a glassy carbon optical transition radiation (OTR) screen was used to record the transversal profile and displacement of the beam [14]. Two Polytec RSV-150 Laser Doppler Vibrometers (LDVs) [18] were used to record the surface velocity of two samples per beam impact through a radiation-hard optical viewport (SCHOTT RS323G19 [19]). By means of a Thermo Scientific MegaRad3 radiation-hard camera (CID8726DX6), samples were observed during the entire experiment. As the LDVs were located roughly 40 meters upstream of the experiment, the LDV lasers were coupled into the chamber and focussed onto the sample's surface using high reflectivity gold mirrors. One set of gold mirrors was mounted on a horizontal translation stage allowing the selection of the two samples to be monitored per requested beam pulse.

2.2. Sample Geometry of Tantalum Core Samples and Overview of Investigated Materials. All samples of target station 6 (see Figure 1(b)) consist of a 10 mm long tantalum rod of 3 mm diameter press fit into a graphitic cylinder of 10 mm outer diameter (see Figure 2(a)). The geometry of short and bulky targets reduces beam-induced bending modes (with large amplitudes) that superimpose with radial and circumferential vibration modes [20–22] and allowed for a compact target station design that could accommodate a large number of different material samples. The fiber-reinforcement plane of all fiber-reinforced targets is oriented normal to the cylinder axis of the samples and thus also normal to the beam axis.
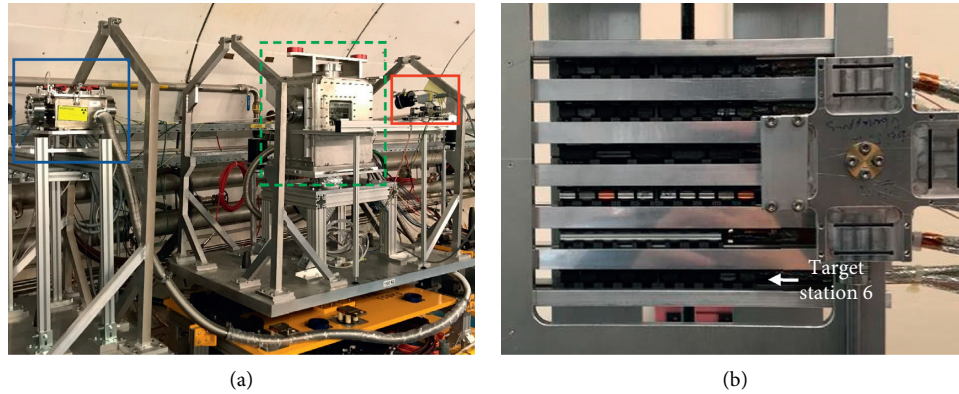
(a) (b)

FIGURE 1: Experimental setup mounted in the HiRadMat irradiation area. The irradiation chamber housing the target holder is indicated by the dashed green frame. The horizontal translation stage with the mirror/rad-hard camera assembly is indicated by the red frame. The beam television (BTV) used to record the transversal beam size is indicated by the blue frame (a). Detailed view of the target holder that hosts the six individual target stations. The cross-shaped object fixed on the right side of the frame holds four sheets of radiation-hard glass to protect the main viewport from potential ejecta (b).
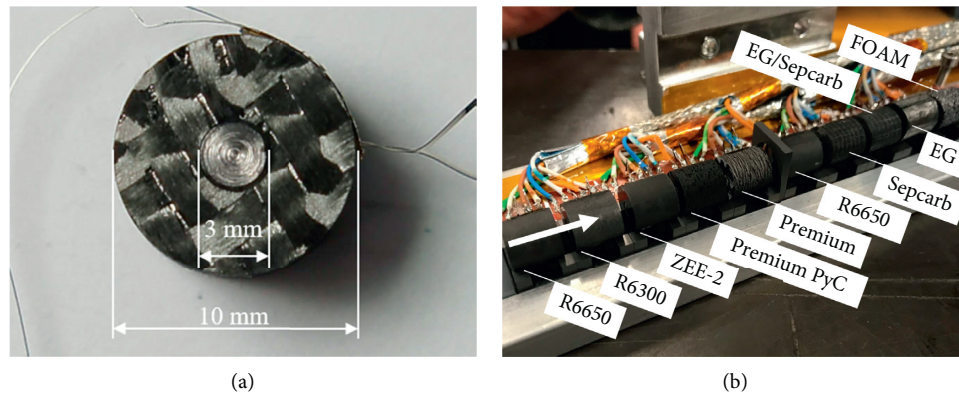

(a) (b)

FIGURE 2: Front face of sample #5 SGL carbon premium with dimensions of the tantalum core (ø3 mm) and surrounding graphite (ø10 mm). The fiber reinforcement is clearly visible and is normal to the cylinder axis (a). Detailed view of the individual samples of target station 6. The arrow on the left indicates the beam direction. More information about the target materials is presented in Table 1 (b).

Each sample was mounted on a polycrystalline graphite (SGL Carbon R6650) support and clamped by another spring-loaded graphite support from the top. Graphite was used as it is quasi transparent to the beam, has strong mechanical damping and high resistance towards mechanical shock [23]. Each sample was preloaded with a force of ~8.3 N by compressing the springs mounted in the top support from their original length of 5.5 mm to 4 mm (spring constant 5.5 N·mm^{-1}). Implicit coupled thermomechanical simulations of the dynamic response in ANSYS show that the samples behave effectively freely suspended when using such a holder configuration.

Overall, 9 different graphitic materials were tested in target station 6 during the experiment (see Figure 2(b)). Table 1 summarizes the different materials in their respective positions along the target station. The choice of materials was based on their usage in beam-intercepting devices of current and future high-power accelerators like FAIR, HL-LHC, or the Future Circular Collider (FCC).

The graphitic materials under study can be grouped into three categories: (i) isotropic polycrystalline graphite, (ii) carbon-fiber-reinforced graphite, and (iii) low-density graphites (≤1 g·cm^{-3}).

(i) Polycrystalline graphite with an average grain size of 7 μm, SGL Carbon R6650 [24], will be used as the production target and beam catchers of the Super-FRS at FAIR [25]. The other tested polycrystalline graphite grades have either larger, 20 μm, SGL Carbon R6300 [24] or smaller, 1 μm, POCO ZEE-2 [26], average grain size.

(ii) Carbon-fiber reinforced graphite (CFC) is currently used as absorber material in the primary and secondary collimators of LHC [1]. SGL Premium [27] has mechanical properties comparable to the material employed in the LHC collimators. During production, SGL Premium PyC undergoes an additional pyrolization treatment that increases its Young's modulus and flexural strength. Another CFC material, ArianeGroup Sepcarb, is going to be used in the collimators of the SPS to High-Luminosity LHC transfer lines at CERN [28]. With

TABLE 1: Overview of target materials. The first column denotes the position of the target along the beam direction (cf. Figure 2(b)). In the second column, μm values for polycrystalline graphites (PG) denote the particle size according to the manufacturer. The flexural strength is determined in three-point bending geometry. $\parallel/\perp$ denotes the respective flexural strength parallel and perpendicular to the fiber-reinforcement plane of carbon fiber reinforced graphite (CFC). The third value for #7 Sepcarb indicates the tensile strength of its graphite matrix. Peak energy deposition values are calculated using FLUKA and represent the peak transversal energy deposition density per primary 440 GeV proton in the tantalum core averaged over the sample length (cf. Figure 3(a)).

#	Target material	Density (g·cm⁻³)	Flexural strength (MPa)	Peak energy deposition in Ta core $(10^{-10}\,\text{J·cm}^{-3}\text{·p}^{-1})$
1	SGL R6650 (PG, 7 μm)	1.84	67	1.7
2	SGL R6300 (PG, 20 μm)	1.73	51	5.5
3	POCO ZEE (PG, 1 μm)	1.77	146	12.9
4	SGL premium PyC (pyrolized 2D-CFC)	1.59	$\parallel$: 123 $\perp$: 290	20.7
5	SGL premium (2D CFC)	1.55	$\parallel$: 106 $\perp$: 225	26.1
6	SGL R6650 (PG, 7 μm)	1.84	67	28.5
7	ArianeGroup sepcarb (3D CFC)	1.5	$\parallel$: 145 $\perp$: 186 17	29.1
8*	Ø 7 mm SGL sigraflex (EG)	1	—	28.8
	Ø 10 mm sepcarb (3D-CFC)	1.5	—	27.9
9	SGL sigraflex (expanded graphite)	1	—	
10	POCO FOAM (graphitic foam)	0.5	3	26.9

*Target #8 comprised two surrounding graphites with the given dimensions.

additional reinforcement by needling, this material exhibits less anisotropy compared to the two-dimensionally reinforced SGL Carbon CFC grades while retaining increased mechanical properties in comparison to polycrystalline graphite [29].

(iii) Low density graphites comprised SGL Sigraflex [30] expanded graphite (EG) (1 g·cm⁻³) and POCO FOAM [31] graphitic foam (GF) (0.5 g·cm⁻³). Expanded graphite (1 g·cm⁻³) is currently employed, e.g., as an absorber in the LHC beam dump [1], but with the foreseen 20-fold increase in stored beam energy of the FCC, graphitic foams (0.5 g·cm⁻³) have emerged as a potential replacement [32]. Furthermore, EG is a candidate material for the surrounding matrix of the upgraded p-bar target at CERN, due to its excellent damping and thermal properties [33, 34]. These types of materials are distinctively different to CFCs and polycrystalline graphite grades due to their large porosity (~78% open porosity in POCO FOAM), strong anisotropy (in-plane thermal conductivity in FG is ~50 times larger than through-plane), and low mechanical strength (3 MPa flexural strength for POCO FOAM).

Tantalum was chosen as core material as it exhibits high atomic number ($Z = 73$), high density ($\rho = 16.6\,\text{g·cm}^{-3}$), high melting temperature (3017°C), and high mechanical strength (~180 MPa tensile strength). Due to the large atomic number and density, the energy deposition density of 440 GeV protons in tantalum (transversal beam profile $\sigma = 1.5$ mm) is up to 13 times larger than the energy deposition density in graphite. Given the large Young's modulus of tantalum (187 GPa) and taking into account the sample geometry of

the tantalum core, beam-induced stresses in the order of ~100 MPa can be expected for a pulse of 2×10^{11} protons ($\sigma = 1.5$ mm, due to a peak temperature increase of $\Delta T_{\text{Ta}} \approx 230$ K) in the tantalum core experiencing the highest energy deposition density in sample position #6 (cf. Table 1). These stresses will couple into the graphite surrounding the tantalum core.

Tantalum was exposed to proton beams in an earlier experiment at the HiRadMat facility under comparable conditions ($\sigma = 1.5$ mm). Among other refractory metals like molybdenum, tungsten [35], and iridium, tantalum shows the highest resistance towards beam impacts. Even though hydrodynamic simulations and neutron tomography revealed the development of internal cracks induced by high-intensity beam impacts, the dynamic response of tantalum is still quasi-elastic up to the highest beam intensity of $\sim 1.7 \times 10^{12}$ protons for a target diameter of 8 mm [20, 34]. Taking the different diameter of 3 mm of the tantalum core of our samples into account, the "limit" for quasi-elastic behaviour of the most loaded tantalum core is estimated to be reached already with $\sim 9 \times 10^{11}$ protons under our experimental conditions.

2.3. Beam Parameters, Data Recording, and Evaluation.

The experiment was conducted at the High-Radiation to Materials (HiRadMat) facility at the Super Proton Synchroton (SPS) of CERN [13, 14]. All samples of target station 6 were impacted by 440 GeV proton beam pulses with intensities between 5×10^{10} and 1.7×10^{12} protons per pulse (ppp). During the experiment, a total of 73 pulses were requested on target station 6. Pulse lengths ranged between 25 and 900 ns. The transversal beam profile is assumed to be Gaussian, characterized by its standard deviation, σ, both in

the horizontal and vertical planes. As mentioned, the transversal profile of the beam intensity and beam position in the horizontal and vertical planes were recorded for each pulse using a glassy carbon-based OTR screen.

The average intensity profile, determined by fitting two Gaussian distributions to the signal of the OTR screen, was $\sigma_H = (1.46 \pm 0.11)$ mm and $\sigma_V = (1.02 \pm 0.09)$ mm in the horizontal and vertical planes. The average beam position deviated by $\pm(0.20 \pm 0.02)$ mm and $\pm(0.02 \pm 0.01)$ mm in the horizontal and vertical planes, respectively (see Figure 4). Together with the metrology of the target station prior to the experiment and the alignment precision of the experimental chamber (≤ 0.1 mm), all samples have been hit on-axis with a maximum deviation of ~0.5 mm in horizontal and ~0.1 mm in vertical planes.

Figure 3(a) shows the calculated peak energy deposition density in the tantalum cores along the stack of sample. Due to the inhomogeneous transversal beam sigma, two different radial temperature profiles along the horizontal and vertical planes should be expected. But, with the build-up of the hadronic shower along the length of the target station, the difference in integrated energy deposition density (in the horizontal and vertical planes) is less than 10% after 20 mm. Therefore, Figure 3(b) shows the radial temperature distribution in the horizontal plane induced by a medium-intensity pulse of 6×10^{11} protons in the center of sample #6. The temperature was calculated in a transient thermal simulation in ANSYS using the energy deposition map calculated by FLUKA for the average beam intensity profile.

For every requested beam pulse, the voltage signal of all bi-axial strain gauges and the surface velocity of two samples were recorded with 4 MHz sampling rate for a total duration of 23 ms (3 ms pre-trigger) using a digital data acquisition system (DAQ) comprising National Instruments PXIe-6124 modules.

Measured and simulated radial surface velocity are analysed using fast Fourier transformation (FFT) after Welch's method [36] yielding power spectral densities with frequency resolutions of 5 and 10 kHz for measurement times of 100 and 200 μs, respectively. For time resolved information about the different beam-induced pressure waves, continuous wavelet transformation (CWT) was applied [37]. If not mentioned otherwise, a complex Morlet wavelet with bandwidth frequency 1.5 and center frequency 1.0 was used for a good compromise between an accurate temporal reconstruction of the signal and a reasonable frequency resolution of about 30 kHz. The resulting heatmaps were normalized and represent the absolute radial surface velocity, hence color bars were omitted.

2.4. Coupled Vibration of Isotropic Cylinders.

Because of the (sub-)μs length of the beam pulses used in the experiment, the energy deposition by the beam leads to "quasi-instantenous" heating. The constrained thermal expansion and related pressure increase of the affected volume leads to the generation of pressure waves that are comparable to a mechanic impact.

To check if the assumption of "quasi-instantaneous" heating is correct, we calculate the characteristic thermal time constant, τ_{ch}, which indicates how long it takes for a physical body (the beam-impacted sample) that has been subjected to a heat pulse of finite thermal energy deposition length, τ_d, (the beam pulse length) to thermalize:

$$\tau_{ch} = \frac{L^2}{a}, \qquad (1)$$

where L is the characteristic length of the physical body and a is its thermal diffusivity. For an isotropic cylinder of radius R and length L submitted to a heat pulse in its center (with constant amplitude along its length), the characteristic thermal time constant is equal to R^2/a. For a tantalum rod with a thermal diffusivity of 24.2 mm·s^{-1} [38] and a radius of 1.5 mm, τ_{ch} is ~100 ms. In comparison to the pulse length of the proton beam (between 25 and 900 ns), the dynamic response of the samples used in this work is governed by the beam-induced "quasi-instantaneous" heating since $\tau_{ch} \gg \tau_d$. Simply said, the samples start to vibrate after beam impact.

The frequencies of certain vibrational modes that are excited by the beam impact can be predicted analytically. Lin [39] introduced several equations that can be used to estimate the fundamental frequencies of the (decoupled) radial and axial vibration of isotropic cylinders that fulfil either $R \gg L$ or $L \gg R$. Assuming plane strain (axial strain is zero), the fundamental radial vibration frequency, f_r, can be obtained by:

$$f_r = \frac{K_r}{2\pi} \sqrt{\frac{E(1-\nu)}{\rho(1+\nu)(1-2\nu)}}, \qquad (2)$$

where K_r is the radial wavenumber, E is the Young's modulus, ρ is the density, and ν is the Poisson's ratio of the cylinder. The radial wavenumber can be obtained by (numerically) solving the following equation:

$$K_r R J_0(K_r R)(1-\nu) - (1-2\nu)J_1(K_r R) = 0, \qquad (3)$$

where J_0 and J_1 are the first kind Bessel functions of zero order and first order. Likewise, under the assumption that radial and tangential stresses are zero while the corresponding strains are present, the axial vibration frequency, f_a, can be obtained by:

$$f_a = \frac{1}{2L} \sqrt{\frac{E}{\rho}}. \qquad (4)$$

Given the geometry of the samples used in this work with $L = 2R$, it should be noted that these equations are not strictly valid. But, we will show that the magnitude of the predicted frequencies is in reasonable agreement with the experimental results.

3. Results and Discussion

Online data recorded by the two Polytec LDVs were analysed yielding surface velocities as a function of time. In the following, selected experimental results together with Fourier and continuous wavelet transformations are

(a)

Time after beam impact:
— 0 μs   — 100 μs
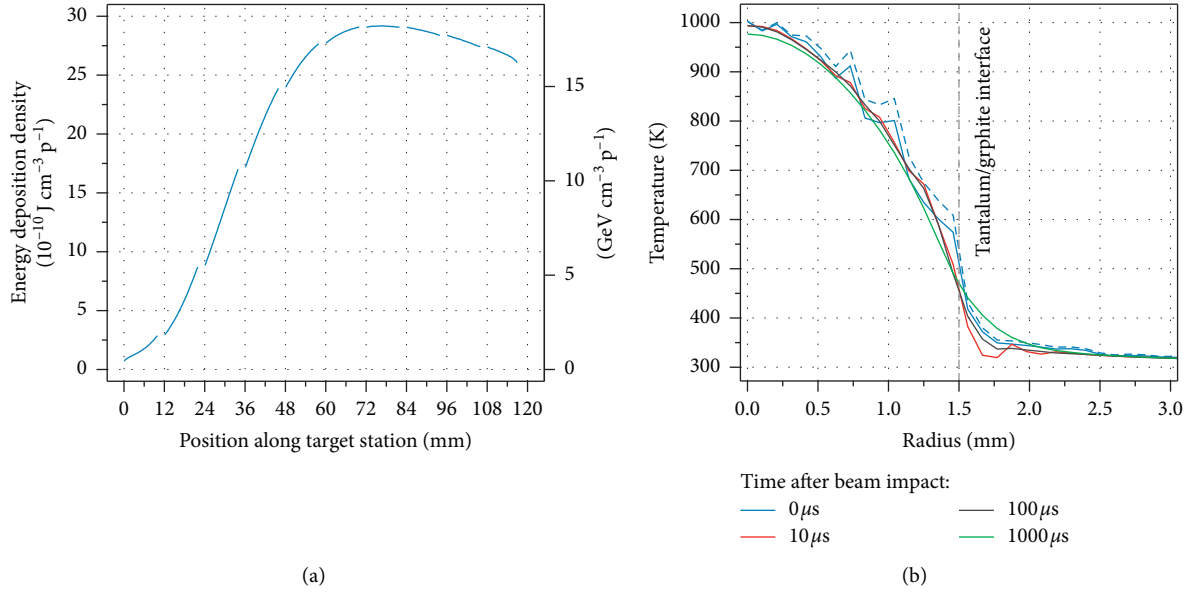— 10 μs   — 1000 μs

(b)

FIGURE 3: Energy deposition density and simulated temperature distribution. Peak energy deposition density in the transversal plane per primary 440 GeV proton for an inhomogeneous Gaussian intensity profile with $\sigma_H = 1.46$ mm and $\sigma_V = 1.02$ mm in the tantalum cores along the length of the sample stack (a). Simulated radial temperature distribution in the horizontal plane and center of sample #6 for different times after beam impact by a single pulse of 6×10^{11} protons (300 ns). The dashed line indicates the radial temperature distribution in the vertical plane directly after beam impact (b).

(a)

■ σ_H
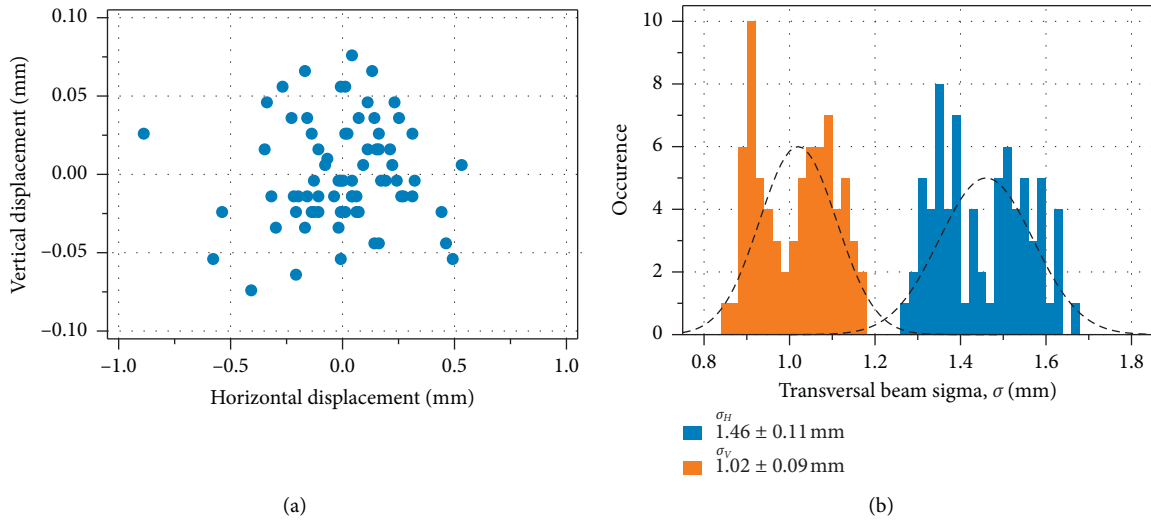 1.46 ± 0.11 mm
■ σ_V
  1.02 ± 0.09 mm

(b)

FIGURE 4: Distribution of the beam position and transversal beam sigma of successive pulses. Displacement of the beam in vertical and horizontal planes for all pulses ($N = 73$) on target station 6 showing severe scattering in the horizontal plane (a). Distribution of the transversal beam sigma in horizontal and vertical planes (b).

presented with the aim of illustrating the general behaviour and specific differences observed for our samples. We also discuss the effect of different beam conditions including (i) low-intensity pulses of $\sim 1 \times 10^{11}$ ppp, where the response of all targets is expected to be in the elastic regime; (ii) medium-intensity pulses of $\sim 6 \times 10^{11}$ ppp, where the beam could have induced failure in several samples; and (iii) high-intensity

pulses of at least 1.2×10^{12} ppp, which lead to significant changes of the dynamic response in all samples, if not failure.

Regarding the different graphites, we concentrate on SGL R6650 (samples #1 and #6) and POCO ZEE (sample #3). SGL R6300 (sample #2) and SGL Premium (#5) are not shown in detail, because they show a similar behaviour as SGL R6650 and SGL Premium PyC, respectively. Samples

comprising expanded graphite (samples #8 and #9) are also not discussed, as their complex structure leads to a complex response yet to be understood.

3.1. Pressure Wave Propagation in Polycrystalline Graphite at 1×10^{11} ppp.

Figure 5 shows the radial surface velocity measured by the LDV on sample #1 SGL R6650 at a pulse intensity of 1×10^{11} ppp (25 ns pulse length). The dynamic response is to a large extent damped within ~0.4 ms. This damping rate is orders of magnitudes faster than the damping observed in pure tantalum. Martin et al. [20] reported damping in pure tantalum, impacted with a similar pulse intensity and transversal beam size, in the order of several tens of milliseconds. Two distinct frequency components, a high frequency component with a period of ~1 μs (~1000 kHz) and a low frequency component of ~9.5 μs (~105 kHz), can be identified in the radial surface velocity signal (cf. Figures 5(a) and 5(b)).

The high frequency component is attributed to the radial pressure wave in the tantalum core, while the low frequency component is emerging due to the axial pressure wave in the tantalum core and graphite shell. Under the assumption that equation (4) can be applied to a two-body cylinder, the calculated axial pressure wave frequencies are 167 kHz (period of ~6 μs) in the tantalum core ($E = 187$ GPa, $\rho = 16.6$ g·cm^{-3}) and 125 kHz (8 μs) in the graphite shell ($E = 12.5$ GPa, $\rho = 1.83$ g·cm^{-3}). Predicting a radial wave period for the entire core-shell target consisting of tantalum and graphite is nontrivial. But, since the energy deposition occurs mainly in the tantalum core (cf. Figure 3), the frequency of the radial pressure wave within the tantalum core can be approximated with equation (2). The calculated radial pressure wave frequency is 987 kHz (~1 μs). It should be stressed that although these frequencies were calculated for isotropic cylinders, the magnitude of frequencies agrees well with the experimental results. An earlier irradiation experiment by Martin et al. has also shown the propagation of the radial pressure wave emerging from a tantalum core through a graphite matrix [34]. The dis- and reappearance of the radial wave (compare the velocity trend prior to and after 150 μs in Figure 5(c)) can be attributed to the emergence of multiple radial wave frequencies. The nonuniform energy deposition density along the axis (cf. Figure 3(a)) and finite pulse length lead to an amplitude-modulated wave.

The mentioned periods and the amplitude-modulation can also be identified in the fast Fourier transformation (FFT) and continuous wavelet transformation (CWT) of the signal that is presented in Figure 6. In the low-frequency range, the axial pressure waves in both tantalum, 167 kHz, and graphite, 125 kHz, can be identified. In the high frequency range, the highest amplitude occurs at a frequency of 970 kHz, relatively close to the predicted radial frequency of 987 kHz with many different high frequency contributions in the range between 850 and 1100 kHz. Other minor contributions occur in the frequency range around ~450 and 650 kHz.

3.2. Numerical Simulation of Sample #1 SGL R6650 at 1×10^{11} ppp.

The response of the sample is expected to be elastic because of the rather low intensity of 1×10^{11} ppp. To verify the numerical reproducibility of such a pulse, a coupled transient thermal and mechanical finite-element simulation was performed in ANSYS Mechanical using quarter geometry of the sample. Temperature- and strain-independent thermal and mechanical material properties were considered for tantalum and SGL R6650 graphite which are summarised in Table 2. The simulation included no damping. The energy deposition by the proton beam was introduced as an internal heat generation. The spatial distribution of the deposited energy was extracted from a FLUKA Monte Carlo simulation [15] using an inhomogeneous Gaussian beam intensity profile with $\sigma_H = 1.46$ mm and $\sigma_V = 1.02$ mm that impacts the sample centrally. The interface between the tantalum core and the graphite shell was approximated using a "rough" contact that allowed separation between the bodies in the radial direction but prohibited sliding along the axis. A more detailed description of the simulation procedure is provided in references [9, 21, 22].

Figure 7(a) shows the comparison between the radial surface velocity obtained from the numerical simulation and the corresponding experimental response for the first 20 μs after beam impact. The radial surface velocity is only slightly overestimated by the simulation and is well in agreement with the experiment for the first ~10 μs after beam impact. It is notable that the maximum surface velocity does not occur within the first oscillation as typically observed for targets of a single material due to the acoustic impedance mismatch between tantalum and graphite. A comparison between the FFT of the experimental and simulated radial surface velocity is shown in Figure 7(b). The simulation does not fully replicate the relative power density of the different frequency components since it does not include any damping. But, the frequency components of the signal are replicated reasonably well. The simulation has its most dominant contribution at ~180 kHz which corresponds to the axial pressure wave, while the contribution from the radial pressure wave at ~990 kHz is severely underestimated. The peak at ~460 kHz is clearly observed at a beam intensity of 6×10^{11} ppp (the dynamic response is shown in Figure 8) but not at 1×10^{11} ppp due to the large differences in damping between those two beam intensities. Furthermore, several peaks between 600 and 850 kHz are present in the simulation but not observed in the experiment.

3.3. Modal Analysis of Sample #1 SGL R6650.

To determine the physical significance of the different frequency components, a modal analysis of the first 2000 natural vibration modes (up to a frequency of ~1000 kHz) was conducted for the sample geometry of sample #1 SGL R6650 in ANSYS Mechanical. Seven vibration modes with frequencies that coincide with the dominant contributions observed in the experimental and simulation results were identified and are compared within Table 3. The opposite deformation cases of these vibration modes are shown in Figure 9. All identified vibration modes have radial symmetry, indicating that these represent fundamental axial vibrations. But, it should be noted that all these vibrations have a radial component. Due
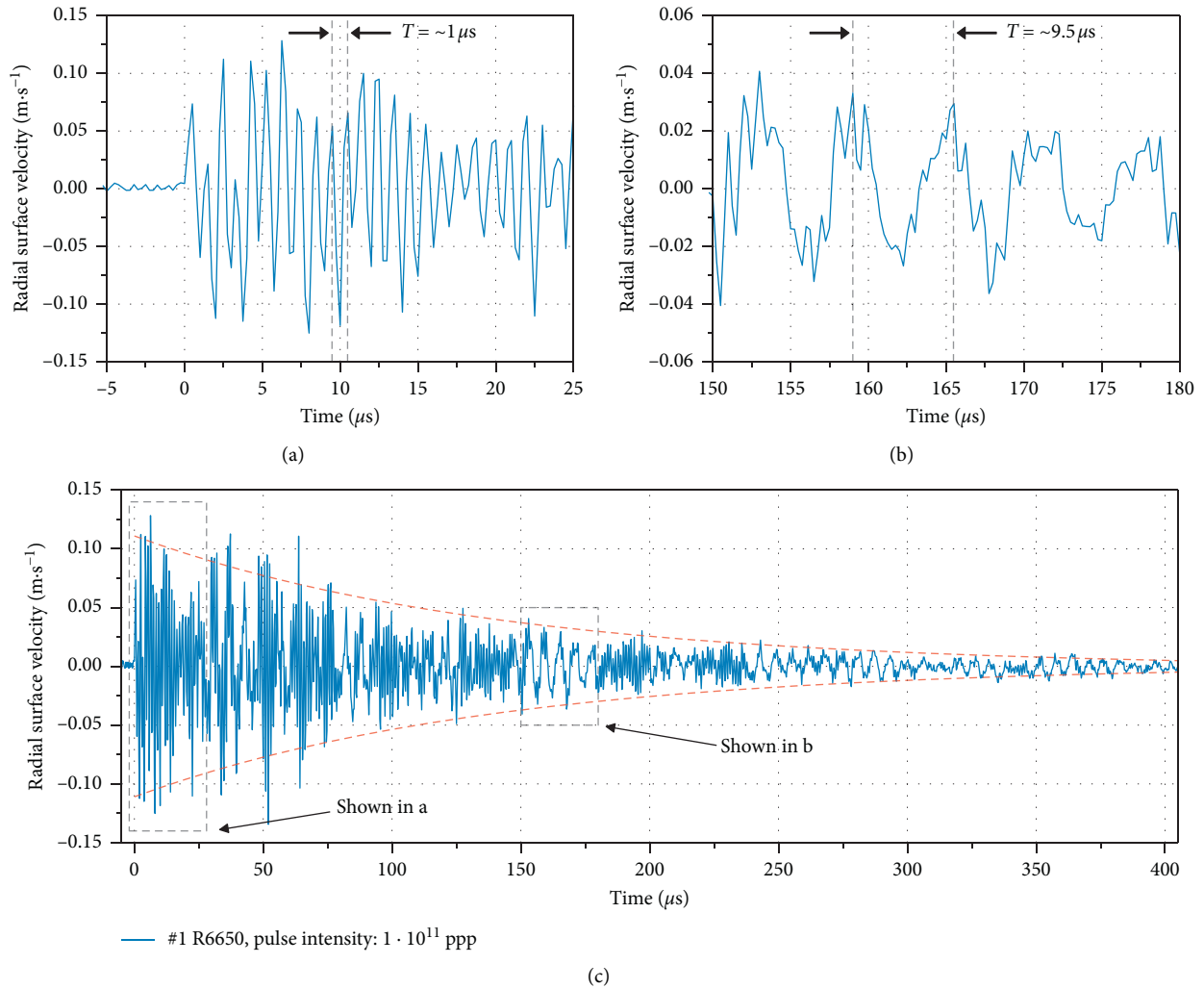
(a)

(b)

(c)

FIGURE 5: Radial surface velocity of target #1 R6650 after impact with 1×10^{11} ppp (25 ns pulse length) as recorded by the LDV. Dynamic response within the first 25 μs after beam impact (a). Response between 150 and 180 μs after beam impact (b). Full response of the target. The dashed red lines represent a guide to the eye for the damping envelope (c).
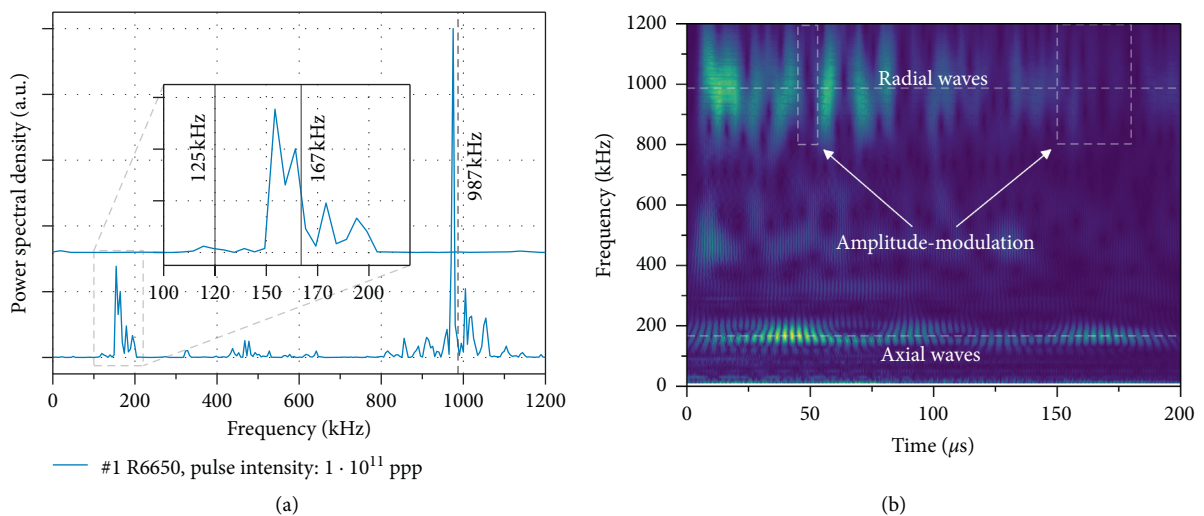

(a)

(b)

FIGURE 6: Frequency analysis of the radial surface velocity of target #1 R6650 after impact with 1×10^{11} ppp within the first 200 μs. The power density as a function of frequency clearly shows the multiple high frequency signals (around 1000 kHz) responsible for the amplitude modulation (a). Continuous wavelet analysis of the absolute radial surface velocity. Color coding represents the values of the normalized absolute radial surface velocity (b).

TABLE 2: Overview of the material properties of tantalum and polycrystalline graphite SGL R6650 used in the coupled transient thermal/transient structural ANSYS simulation.

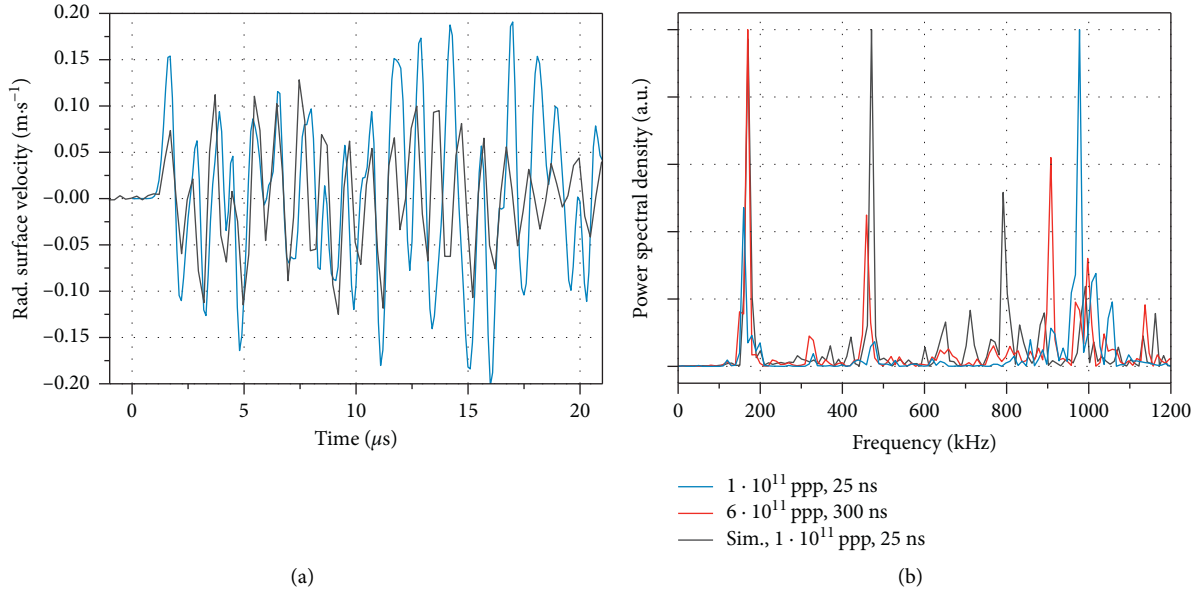| Material property		Tantalum	Graphite
Density (g·cm^{-3})	ρ	16.6	1.83
Specific heat capacity (J·g^{-1}·K^{-1})	c_p	0.151	0.7
Young's modulus (GPa)	E	187	12.5
Coefficient of thermal expansion (K^{-1})	α	6.5×10^{-6}	4.2×10^{-6}
Poisson's ratio	ν	0.35	0.18
Thermal conductivity (W·m^{-1}·K^{-1})	k	54	95

(a)

(b)

FIGURE 7: Comparison between experimental and simulation results for sample #1 SGL R6650. Experimental (black) and simulated (red) radial surface velocity as a function of time for 20 μs after beam impact for a beam intensity of 1×10^{11} ppp (a). Normalized power spectral densities for the first 100 μs after beam impact of the simulation and the experiment at two different beam intensities (b).

to the sample geometry where $L = 2R$, coupled vibrations can be expected to be the dominant contribution to the dynamic response.

Experimental and simulation results were analysed by continuous wavelet transformation to compare whether the different frequency components can be unambiguously identified in the experimental signal and are not simply noise in the FFT. The resulting heatmaps, superimposed with the FFTs, are shown in Figure 10. In this case, a complex Morlet wavelet with bandwidth frequency 4 and center frequency 5 was used that lead to a frequency resolution of ~10 kHz which make the CWTs directly comparable to the FFT. Although this comes at the cost of smaller temporal reproducibility, e.g., the amplitude modulation of the radial pressure wave at ~50 μs cannot be identified in comparison to Figure 6 for the beam impact with 1×10^{11} ppp. But, the CWTs clearly show that the frequency components of the simulation are well in agreement with the experiment. Hence, we conclude that the differences between the FFTs of the simulation and the experimental results are largely due to the different damping of the different vibration modes.

3.4. Pressure Wave Propagation in Polycrystalline Graphites at 1×10^{11} and 6×10^{11} ppp. Figure 8 shows the radial surface velocity measured by the LDVs for beam impacts with intensities of 1 and 6×10^{11} ppp in different graphite samples (a) #1 R6650, (b) #6 R6650, and (c) #3 POCO ZEE. At a beam intensity of 1×10^{11} ppp, the three materials exhibit similar signals that are dominated by the high-frequency radial pressure wave of the tantalum core (~1000 kHz). The difference in the maximum observed velocity (~0.1 m·s^{-1} for #1 R6650 and ~1 m·s^{-1} for #6 R6650) scales linearly with the ratio between the energy deposition density (~12) in the tantalum cores of the two samples (see Table 1), indicating fully elastic response of the targets at this beam intensity.

At 1×10^{11} ppp, the response of #6 R6650 exhibits a degree of amplitude-modulation not observed in any other measurements. As the sample was being hit eccentrically by the beam with a horizontal offset of 0.23 mm and 0.13 mm vertical offset (~5% of the radius), beam-induced bending modes (typical frequencies would be below the axial pressure wave frequency, <100 kHz) were suspected, but no low-frequency signal was observed in either the FFT or CWT of the signal. One can only assume that large beam offsets
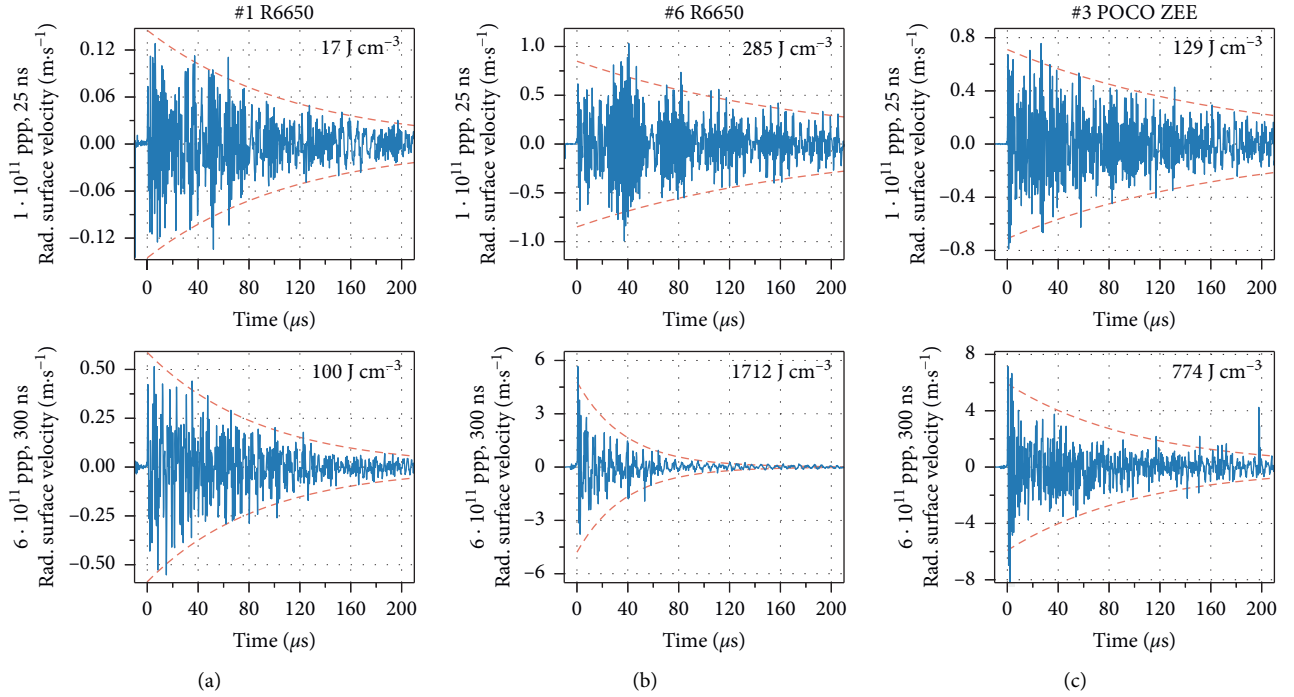
FIGURE 8: Recorded surface velocity (solid blue line) and calculated damping envelope (red dashed line) as a function of time up to 200 μs after beam impact. (a–c) compares three different polycrystalline graphite samples: #1 SGL R6650 (a), #6 SGL R6650 (b), and #3 POCO ZEE (c) at 1×10^{11} ppp (top) and 6×10^{11} ppp (bottom) beam intensity. The energy density provided in each plot indicates the peak energy deposition in the tantalum core averaged over the length of the sample.

TABLE 3: Comparison of frequency components identified in the FFT of the experimental results, the FFT of the simulations for a beam intensity of 1×10^{11} ppp, and modal analysis of the target geometry. Frequencies obtained from FFT have a systematic error of ± 10 kHz.

Experiment FFT (kHz)		Simulation FFT (kHz)	Modal analysis (kHz)
1×10^{11} ppp	6×10^{11} ppp	1×10^{11} ppp	
160	170	170	153.4/186.4
330	330	330	319.5
460	470	480	477.3
-		810	800	804.0
910	910	880	899.7
980	990	980	978.4

induce stronger amplitude modulation in multi component targets with an acoustic impedance mismatch.

The damping time constant, τ, was extracted using an exponential decay function (indicated by the damping envelope shown in Figure 8) for the overall dynamic response. As detailed in the previous section, the dynamic response is composed of various vibration modes. To compare the trend of the overall damping of target #1 SGL R6650 with the frequency-related damping, time constants were extracted by CWT of the dynamic response for the six most dominant vibrations, which were also identified by modal analysis. The damping time constants for these vibrations and their frequencies are shown in Figures 11(a)–11(f). The largest time constants are observed for the lower frequencies of 170 kHz and 330 kHz, but no systematic correlation between higher

frequencies and decreasing time constant can be identified. All time constants steadily decrease with increasing pulse intensity.

An identical trend is also observed when comparing the damping between the different PG samples, which is shown in Figure 11(g). There is no obvious correlation between graphitic microstructure and damping. This is surprising because one would have expected that the internal damping of the PGs is considerably affected by their different particle size. Smaller particle sizes should lead to increased internal friction and therefore higher damping. The complex target geometry and the high frequencies (which inherently have high damping) of the dominating radial pressure waves may cancel possible particle size effects. Hence, the steep increase in damping between 1×10^{11} and 6×10^{11} ppp is tentatively attributed to the beam-induced temperature increase in the tantalum cores. Similar behaviour (increased damping with increasing pulse intensity and therefore sample temperature) has been observed in pure tantalum in [20].

Figure 12 shows the normalized FFT spectra of the dynamic response data presented in Figure 8. As discussed above, the signal composition does not change significantly at higher pulse intensities, except for the radial pressure wave signal ascribed to the tantalum core (at ~1000 kHz) which almost vanishes under the impact of 6×10^{11} ppp on #6 R6650 (b). Due to their specific displacement vectors, it is not expected that the axial pressure wave can be identified, but not the radial pressure wave. Figure 13 shows the CWT of the dynamic response for 100 μs after beam impact. The high frequency radial pressure wave signal is still observable
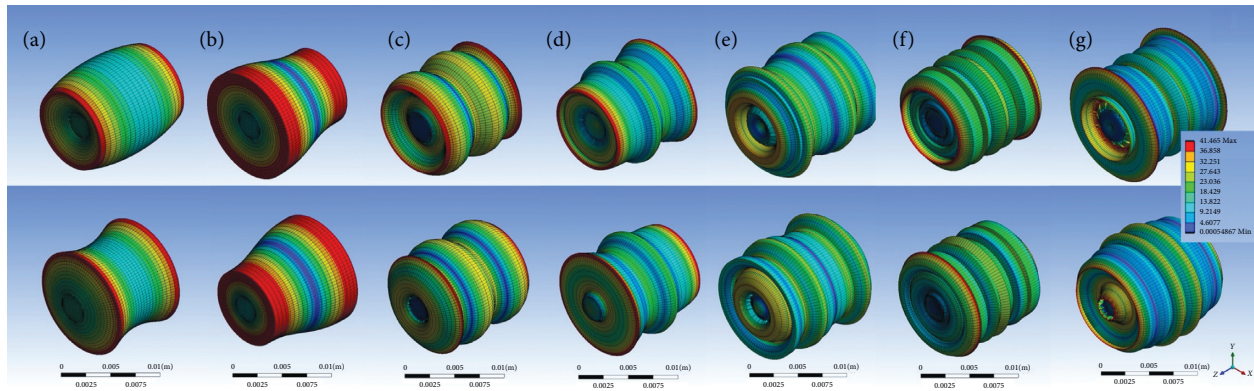
FIGURE 9: Qualitative opposite extreme deformation (top and bottom) of different vibration modes obtained by modal analysis of sample #1 SGL R6650 that coincide with dominant frequency contributions were measured during the experiment. The vibration modes have frequencies of 153.4 (a), 186.4 (b), 319.5 (c), 477.3 (d), 804.0 (e), 899.7 (f), and 978.4 kHz (g). Color coding qualitatively represents the normalized magnitude of deformation. Scale bars correspond to 10 mm.
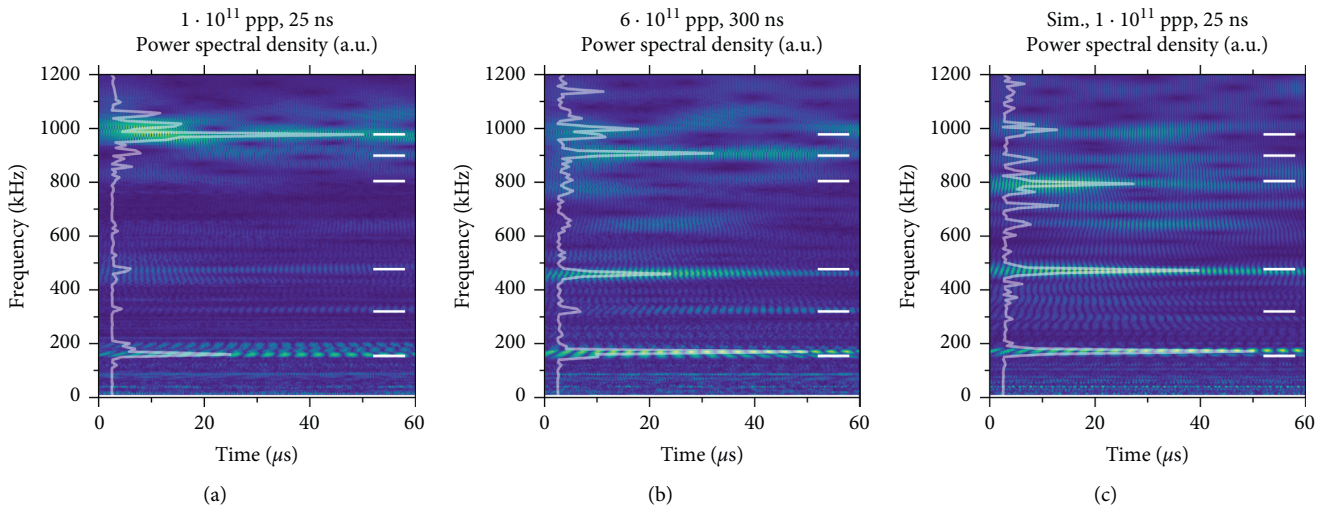

FIGURE 10: Continuous wavelet transformation of the radial surface velocity obtained in the experiment and by simulation for sample #1 SGL R6650. The normalized power spectral density plot is overlaid in light grey. Solid white lines indicate vibration modes of the target geometry obtained by modal analysis. Experimental result at 1×10^{11} ppp (a), 6×10^{11} ppp (b), and simulation result at 1×10^{11} ppp (c).

in the CWT as opposed to the FFT (cf. Figure 12). This shows that the damping depends strongly on the frequency of the signal and the high frequency radial pressure wave is damped within ~20 μs, as opposed to the low frequency axial pressure waves that can be observed even beyond 100 μs.

3.5. Pressure Wave Propagation in CFCs and Graphitic Foam at 1×10^{11} and 6×10^{11} ppp.
Figure 14 shows the radial surface velocity after beam impacts with intensities of 1×10^{11} and 6×10^{11} ppp in samples (a) #4 SGL Premium PyC, (b) #7 ArianeGroup Sepcarb, and (c) #10 POCO FOAM. The response of the fiber-reinforced graphites (CFCs) and the graphitic foam differs significantly from the response of the isotropic polycrystalline graphite samples discussed in previous section (cf. Figure 8). Measured

maximum surface velocities are considerably smaller at comparable energy densities deposited in the tantalum cores. In both CFCs, samples #4 Premium PyC and #7 Sepcarb, the maximum surface velocity increased only by a factor of ~2.5 when increasing the beam intensity from 1×10^{11} to 6×10^{11} ppp.

Both CFCs exhibit considerably stronger damping with time constants <100 μs in comparison to the PGs. Fiber-reinforcement planes consist of individual fibers that are bundled together in so-called rovings, which are then woven into mats that are interconnected by a discontinuous graphite matrix. Hence, the increased damping of the CFCs is probably due to the large number of interfaces. Moreover, the average pore volume of CFCs is larger than in PGs because of the lower density of CFCs. Surprisingly, POCO FOAM has a damping time constant in the order of ~200 μs

(a)

(b)

(c)

(d)

(e)

(f)

(g)

- - ■ - - #1 SGL R6650
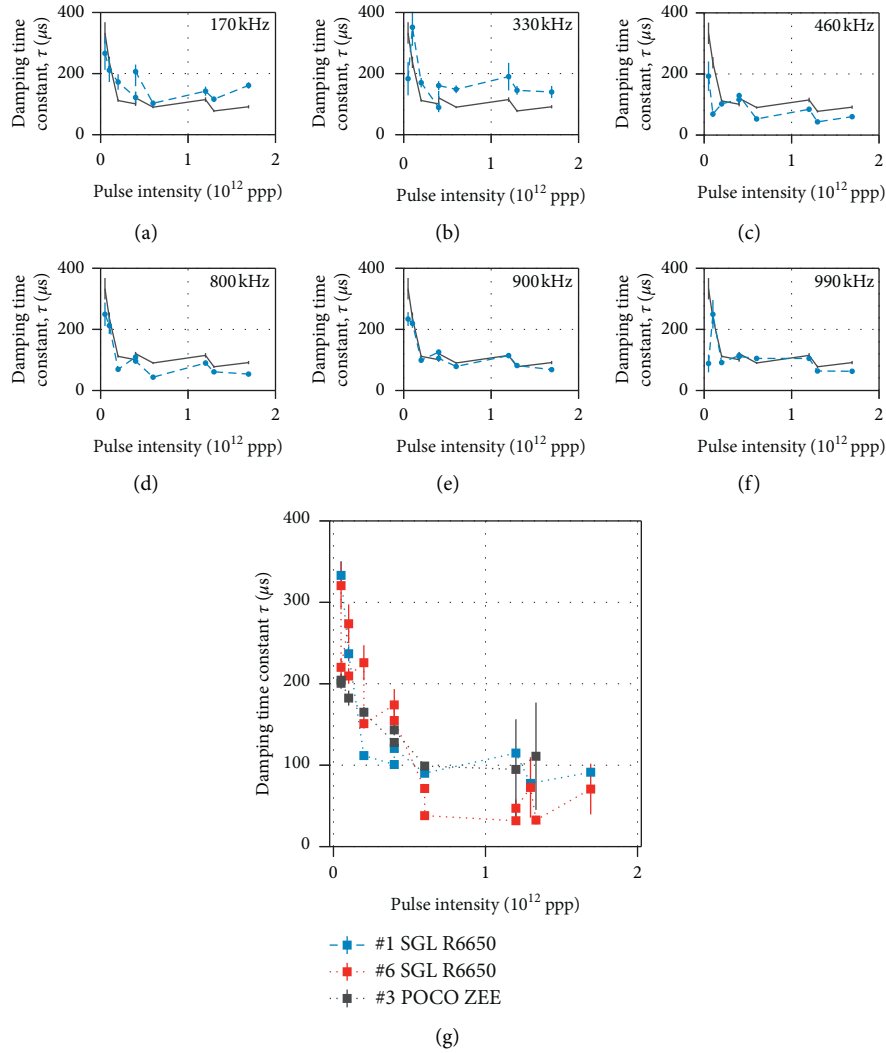· · ■ · · #6 SGL R6650
· · ■ · · #3 POCO ZEE

FIGURE 11: Evolution of the damping time constant, τ. Damping time constant as a function of beam intensity for different frequency components (blue markers) of sample #1 SGL R6650 obtained from continuous wavelet analysis in comparison to the damping time constant (black line) of the radial surface velocity (a–f). Damping time constant of the radial surface velocity for samples #1 SGL R6650, #6 SGL R6650, and #3 POCO ZEE as a function of pulse intensity (b).
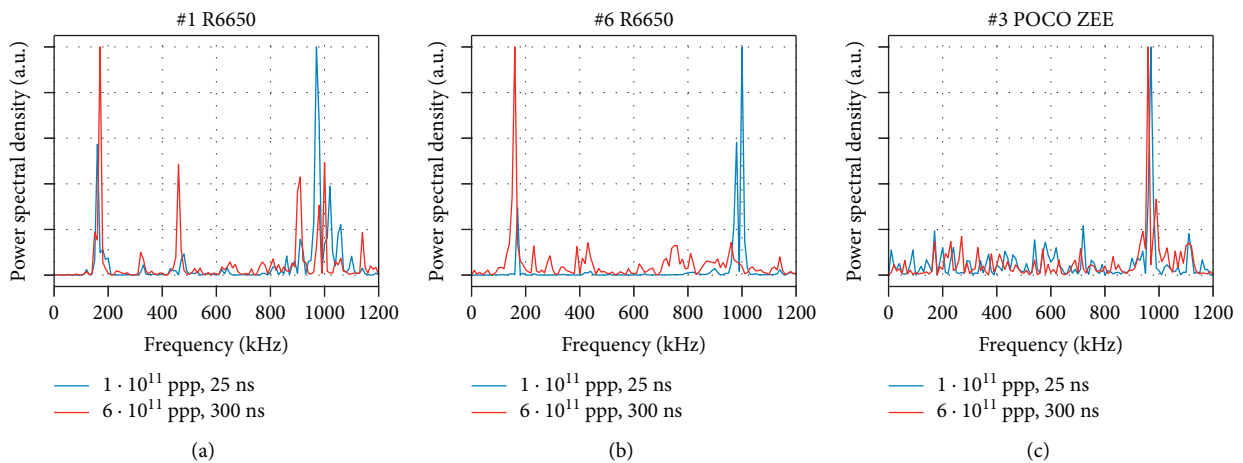

#1 R6650

#6 R6650

#3 POCO ZEE

—— $1 \cdot 10^{11}$ ppp, 25 ns
—— $6 \cdot 10^{11}$ ppp, 300 ns

—— $1 \cdot 10^{11}$ ppp, 25 ns
—— $6 \cdot 10^{11}$ ppp, 300 ns

—— $1 \cdot 10^{11}$ ppp, 25 ns
—— $6 \cdot 10^{11}$ ppp, 300 ns

(a)

(b)

(c)

FIGURE 12: Frequency analysis of the radial surface velocity presented in Figure 8. The normalized power density within the first $100\,\mu$s after beam impact is shown for beam impacts with intensities of 1 and 6×10^{11} ppp of samples #1 SGL R6650 (a), #6 SGL R6650 (b), and #3 POCO ZEE (c).
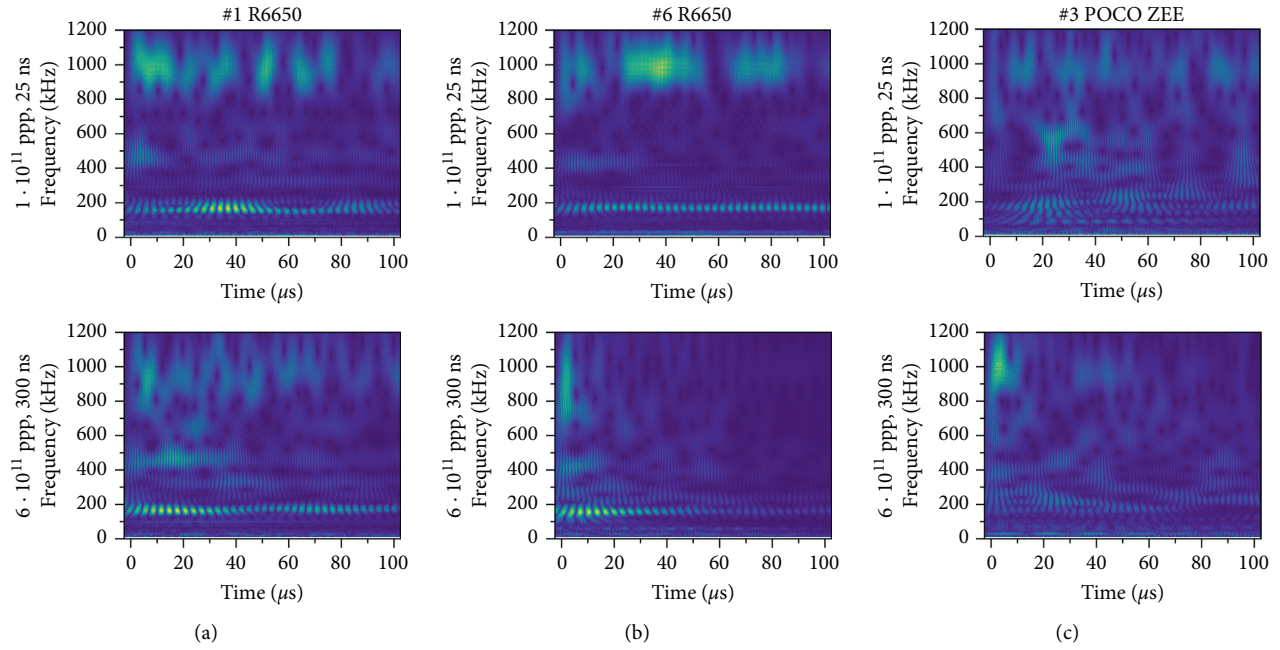
FIGURE 13: Continuous wavelet transformation of the radial surface velocity presented in Figure 8. (a–c) compares three different polycrystalline graphite samples (#1 SGL R6650 (a), #6 SGL R6650 (b), and #3 POCO ZEE (c)) at low and medium pulse intensity (1×10^{11} ppp (top) and 6×10^{11} ppp (bottom)).
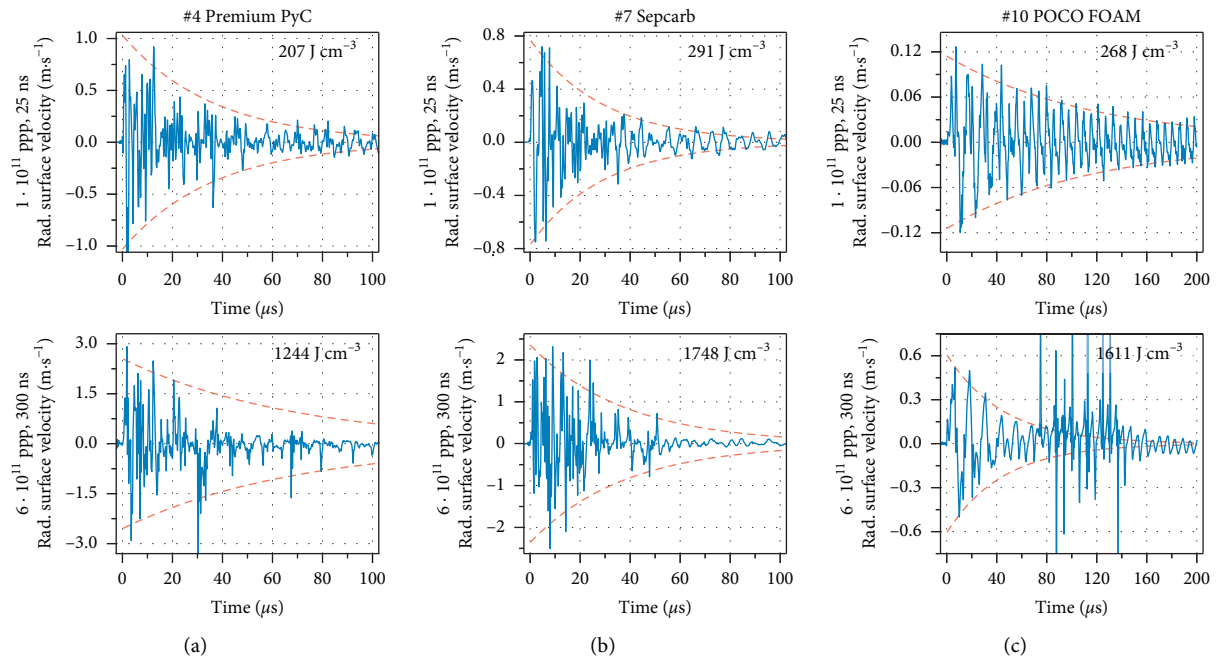

FIGURE 14: Recorded radial surface velocity (solid blue line) and calculated damping envelope (red dashed line) as a function of time for 100 and 200 μs after beam impact. (a–c) Compares two different carbon-fiber reinforced graphite composite and graphitic foam: #4 SGL Premium PyC (a), #7 ArianeGroup Sepcarb (b), and #3 POCO FOAM (c) at 1×10^{11} ppp (top) and 6×10^{11} ppp (bottom) pulse intensity. The energy density provided in each plot indicates the peak energy deposition in the tantalum core averaged over the length of the sample. The perturbations in (c) are nonperiodic.

although it has the lowest density (less than ~30% of the PGs), largest porosity (~75%), and macroscopic pore size of several hundreds of micron diameter [40].

Figure 15 shows the frequency analysis of the dynamic response. Both CFCs exhibit a large number of super-imposed frequencies (cf. Figures 15(a) and 15(b)), which is
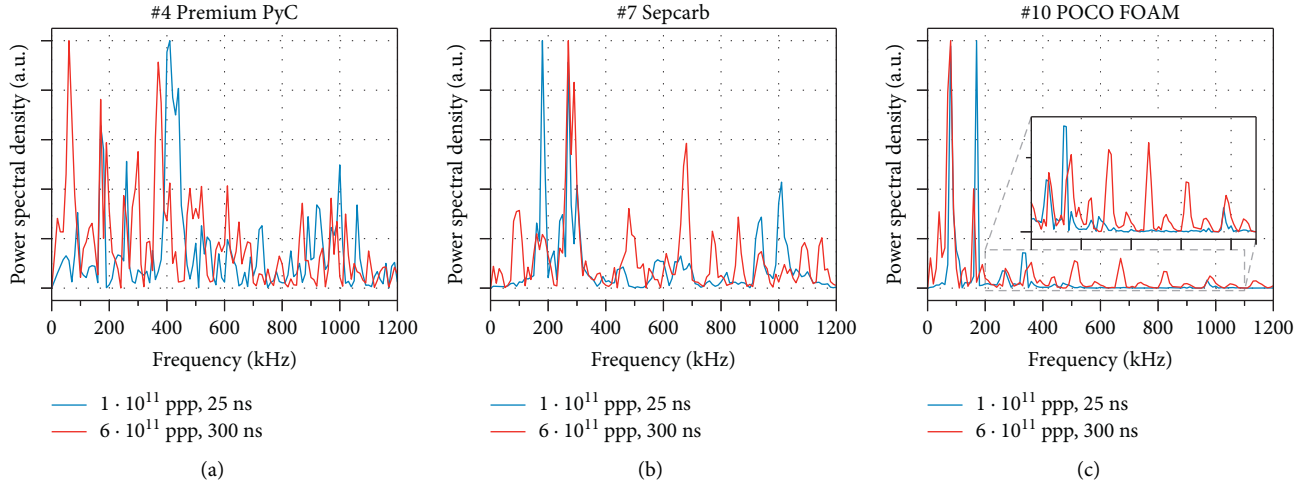
FIGURE 15: Frequency analysis of the radial surface velocity presented in Figure 14. The normalized power density within the first 100 μs after beam impact is shown for beam impacts with intensities of 1×10^{11} and 6×10^{11} ppp of samples #4 Premium PyC (a), #7 Sepcarb (b), and #10 POCO FOAM (c). The inset in (c) shows the zoomed region in which the split radial signal is expected.
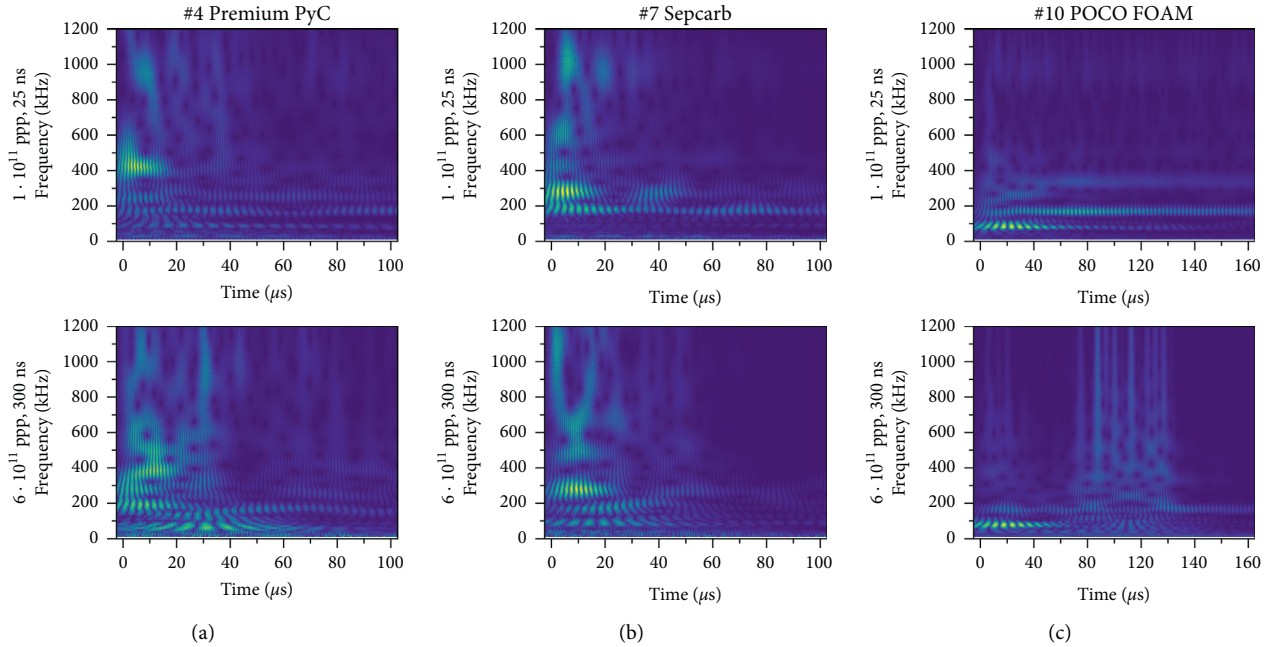

FIGURE 16: Continuous wavelet transformation of the radial surface velocity presented in Figure 14. (a–c) Compares two different carbon-fiber reinforced graphite composite and graphitic foam: #4 SGL Premium PyC (a), #7 ArianeGroup Sepcarb (b), and #3 POCO FOAM (c) at 1×10^{11} ppp (top) and 6×10^{11} ppp (bottom).

explained by the anisotropy of the CFCs ($E_\perp / E_\parallel \approx 5$ in Sepcarb [29]) that leads to complex pressure wave superposition. In contrast to the PGs (cf. Figure 12), the high frequency radial pressure wave of the tantalum core is rather small and broad in #4 Premium PyC and #7 Sepcarb and is suppressed in sample #10 POCO FOAM. The continuous wavelet analysis of these samples is presented in Figure 16 and, as observed in the PGs, the radial pressure wave of the tantalum core is amplitude-modulated and due to the strong damping hard to identify in the velocity signal. The absence of a clear radial pressure wave in #10 POCO FOAM can be

explained by the large acoustic impedance mismatch between tantalum and POCO FOAM ($E = 0.4$ GPa [41], $\rho = 0.5$ g·cm^{-3}), which leads to a splitting of the radial signal into multiple components (cf. inset of Figure 15(c)).

3.6. Material Response at High Intensities. Figure 17 shows the samples' response as recorded by the LDV for the highest requested beam intensities (1.2–1.7 × 10^{12} ppp) during the experiment. The dynamic response degraded quite dramatically. The maximum surface velocity does not follow the
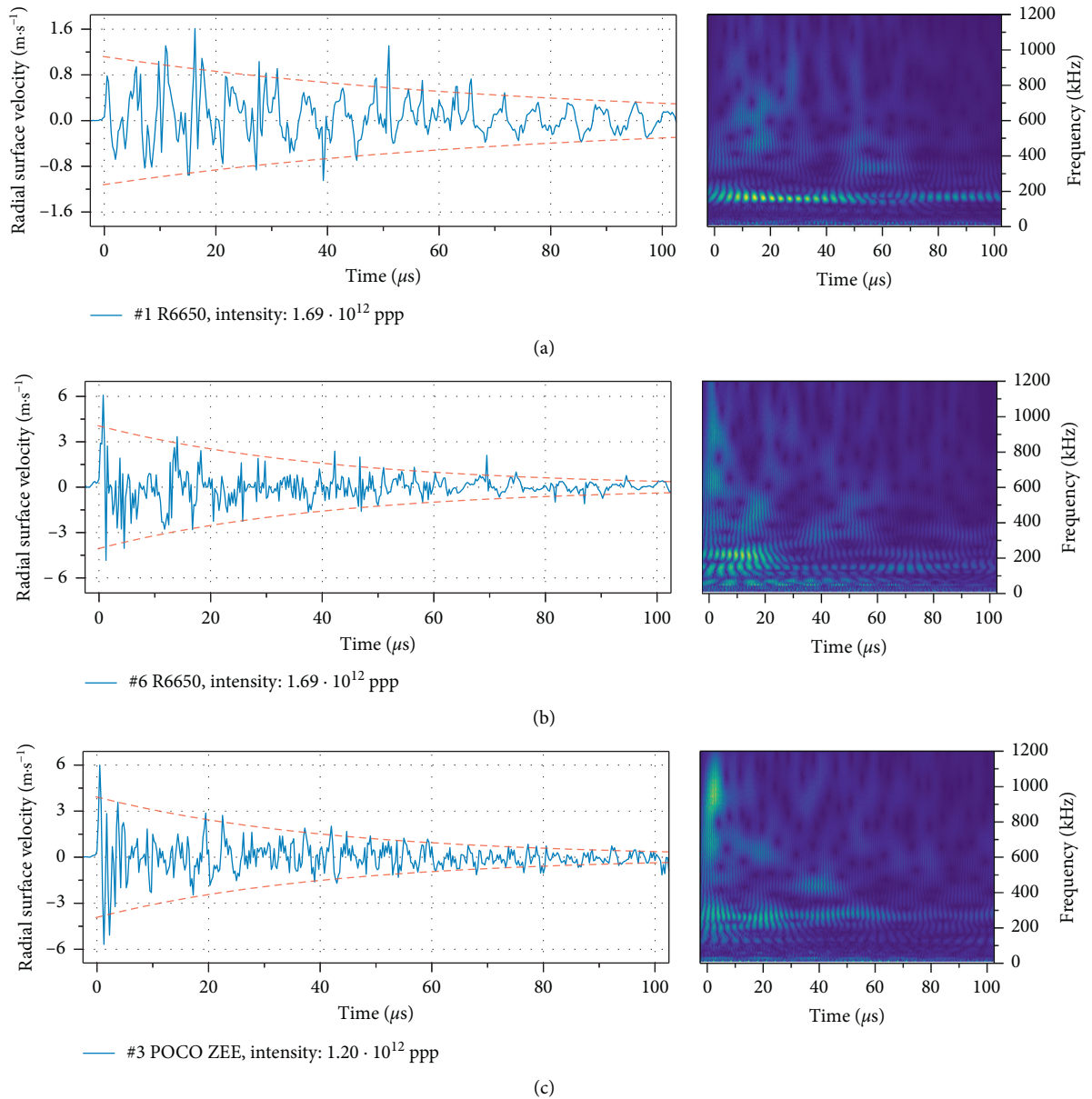
(a)

(b)

(c)

FIGURE 17: Radial surface velocity for maximum applied beam intensity on sample #1 R6650 (a), #6 R6650 (b), and #3 POCO ZEE (c). Left: recorded surface velocity (solid blue line) and calculated damping envelope (red dashed line). Right: continuous wavelet transformation as a function of time up to $100\,\mu$s after beam impact.

beam intensity linearly, except for #1 R6650 (cf. Figure 8). Radial surface velocities of target #6 R6650 should be above $10\,\mathrm{m\cdot s^{-1}}$ (see maximum surface velocity at 6×10^{11} ppp (Figure 8(b)) compared with 1.69×10^{12} ppp (Figure 17(c)). Also, for #3 POCO ZEE, the surface velocity under high intensity is unexpectedly low. It can safely be assumed that failure has occurred in targets #3 POCO ZEE and #6 R6650. This is also indicated by the severe "deformation" of the first oscillation of the dynamic response in #6 R6650 and the large difference between the absolute maximum and minimum surface velocity (indicating loss of energy by plastic deformation or failure). Determining an exact intensity, or energy deposition density, limit below which no material failure should be expected is difficult. Due to the target

station layout, all samples are being impacted in-line and the observed material behaviour is determined by the cumulative effects of several beam impacts.

It is important to note that even under such high beam intensities, the axial pressure wave of the tantalum core is observed for all targets, indicating that the mechanical interface between core and shell is still functional to a certain degree. This is also supported by the presence of the radial pressure wave, albeit that the frequency response is heavily "smeared" compared to the response at lower beam intensities.

Figure 18 shows the radial surface velocity of the anisotropic targets #4 Premium PyC, #7 Sepcarb, and #10 POCO FOAM induced by the highest beam intensities during the experiment. Again, in contrast to the low and
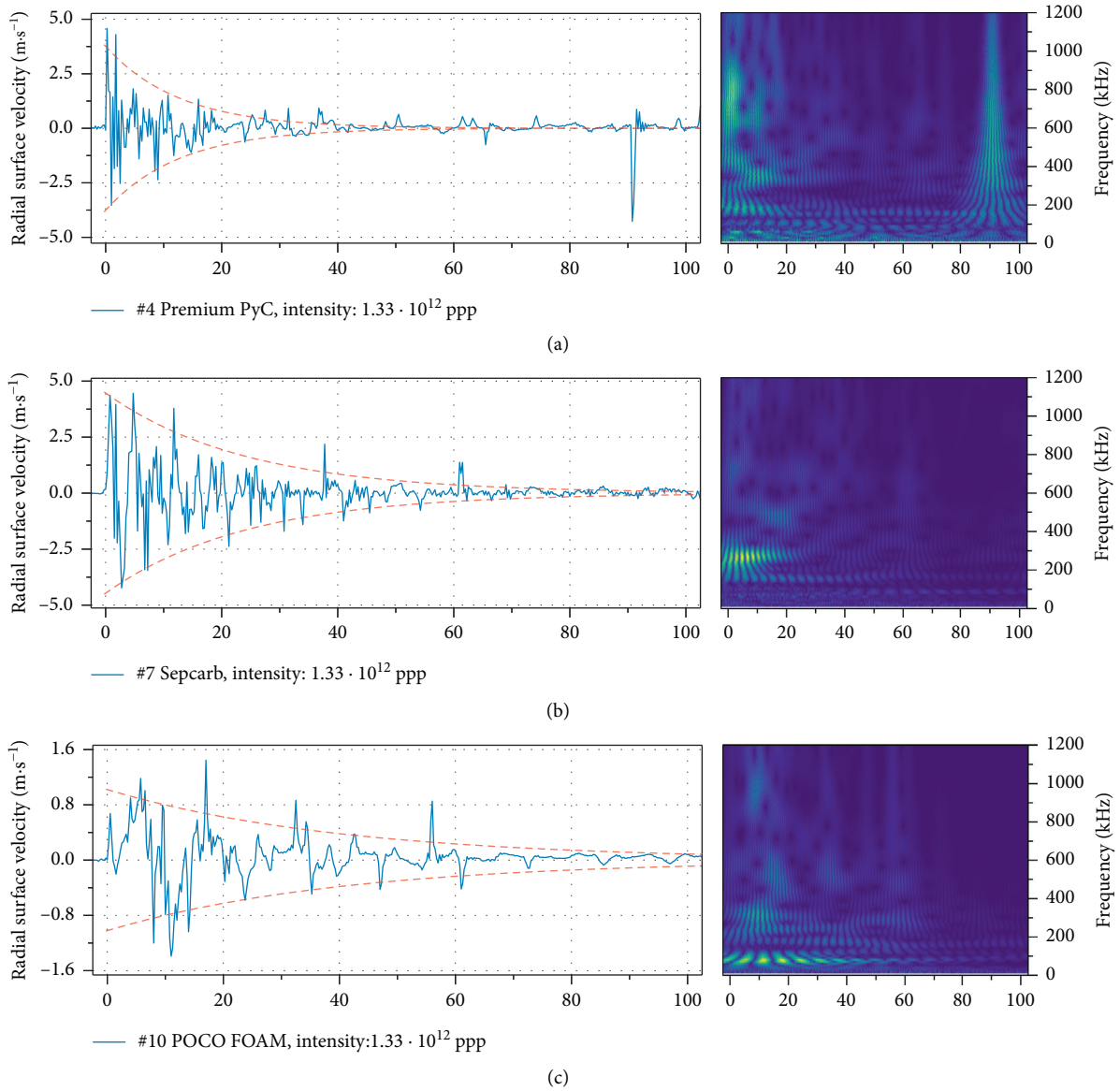
Figure 18: Radial surface velocity for maximum applied beam intensity for samples #4 Premium PyC (a), #7 Sepcarb (b), and #10 POCO FOAM (c). Left: recorded surface velocity (solid blue line) and calculated damping envelope (red dashed line). Right: continuous wavelet transformation as a function of time up to $100\,\mu$s after beam impact.

medium intensity beam impacts shown in Figure 14, dramatic changes in the sample's response are observed. The absolute maximum and minimum surface velocities in samples #4 Premium PyC and #10 POCO FOAM are very different. For samples #7 Sepcarb and #10 POCO FOAM, the maximum surface velocity still increases nearly linear with beam intensity (cf. Figure 14). #7 Sepcarb shows the "cleanest" response at high beam intensities, but failure cannot be completely excluded because of the deformation of the individual oscillations.

3.7. Summary of Macroscopic Material Response. The energy density deposited into the tantalum core of different samples depends on the position along the target station and is

deduced from FLUKA simulations considering the size and intensity of the primary beam as well as the production of secondary particles (cf. Table 1 and Figure 3(a)). Due to the complex wave superposition given by the tantalum core/graphite target geometry, the highest radial surface velocity might occur after the first oscillation has reached the surface. Figures 19(a) and 19(b) show the absolute maximum radial surface velocity reached within $20\,\mu$s after beam impact as a function of energy deposition density in the tantalum core.

Assuming elastic response of the tantalum core and the surrounding graphite, the radial surface velocity increases with the energy deposition density (or in the frame of one target, with the beam intensity). The scattering of the data has probably several reasons including the variation of the horizontal and vertical positions of the beam (cf. Figure 4).
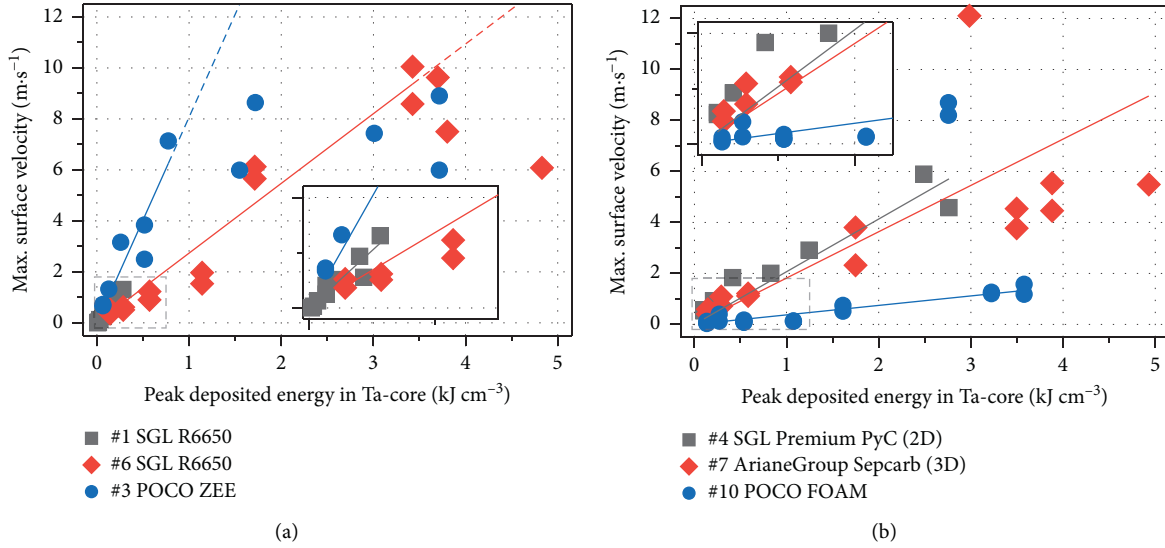
FIGURE 19: Recorded maximum surface velocity. Absolute maximum surface velocity (symbols) as a function of deposited energy in the tantalum core for targets #1, #3, and #6 (a) and targets #4, #7, and #10 (b). Insets are blow-ups of the dashed boxes. Lines represent a guide to the eye for the proposed range of deposited energy where the sample shows an overall elastic response. Error bars are smaller than the symbols.

Sublinear surface velocities at highest beam intensities are ascribed to material failure (indicated by the dashed line in Figure 19(a)). Tantalum should exhibit a quasi-elastic response up to a beam intensity of at least $\sim 9 \times 10^{11}$ ppp in the most loaded sample position #7, which corresponds to an energy deposition density of ~ 2.6 kJ·cm^{-3}. For the two SGL R6650 polycrystalline graphite targets (#1 and #6), the evolution of the maximum surface velocity follows nearly the same trend, as expected. For energy deposition densities larger than ~ 3.5 kJ·cm^{-3}, the velocities are smaller than the linear trend.

The dynamic response of the carbon-fiber-reinforced graphites #4 Premium PyC and #7 Sepcarb is shown in Figure 19(b). Both CFCs exhibit significantly smaller maximum surface velocities of up to ~ 6 m·s^{-1} in comparison to the polycrystalline graphite samples (maximum surface velocity ~ 10 m·s^{-1}). At energy deposition densities below 1 kJ·cm^{-3}, the samples seem to follow the same trend (cf. inset of Figure 19(b)) followed by a sublinear behaviour at higher energy densities. We do not expect that this is due to catastrophic failure but rather ascribe the effect to the low-strength matrix. Even though the investigated CFCs have the highest flexural strength of the materials studied in this work (see Table 1), the tensile strength of the graphite matrix in Sepcarb is only 17 MPa [29]. Structural integrity (indicated by linear behaviour at high energy deposition densities) is therefore provided by the fiber reinforcement, but local failure can readily occur in the low strength graphite matrix and at the interface between fiber reinforcement planes and the matrix, as indicated by the same trend at low energy deposition densities.

The macroscopic response of #10 POCO FOAM, shown in Figure 19(b), is rather peculiar, as it fully follows a linear trend. Since POCO FOAM has a flexural strength of only 3 MPa, catastrophic failure was expected already at low pulse

intensities. Even though the response degraded dramatically at high intensities (cf. Figure 18(c)), the response between 1×10^{11} ppp and 6×10^{11} ppp was virtually unchanged (cf. Figure 14(c)). This is probably the most surprising result of this work and is indicating that low-density graphitic foam might be a good candidate for high power beam dumps as the low density leads to a significant dilution of the energy deposition density.

4. Conclusions

This work presents the experimental results and simulations regarding the dynamic response to intense proton pulses of 9 different graphite materials with a tantalum core. Each sample was impacted with 440 GeV proton pulses with consecutively increasing intensities ranging from 5×10^{10} up to 1.7×10^{12} protons per pulse. Considering the different energy deposition densities that the samples are exposed to, a maximum energy deposition density of ~ 5 kJ·cm^{-3} was achieved in the tantalum core.

The beam-induced stresses and strains in the tantalum core are propagating as elastic pressure waves through the material and are coupling into the surrounding graphite. The radial and axial pressure waves in the tantalum core and in the surrounding graphites were identified by laser Doppler vibrometry and agree with analytical predictions.

By systematically increasing the beam intensities, we find a linear increase of the surface velocity as a function of deposited energy density. Sublinear velocities are interpreted as an indication of material failure. For polycrystalline graphite SGL R6650 surrounding the most loaded tantalum core, the first signs of failure were identified for pulse intensities of $\sim 6 \times 10^{11}$ ppp (~ 1.8 kJ·cm^{-3}). We have also shown that FEM simulations using ANSYS Mechanical, conducted with temperature-independent material

properties, are able to replicate the dynamic response at low beam intensities. Together with the dynamic response measured on bare graphite targets (not presented here), the presented results form a basis to develop more sophisticated material models, e.g., benchmarking of equation of state in ANSYS AUTODYN for isotropic graphite at larger beam intensities in view of onsetting and/or gradual material failure.

The geometry of the investigated targets, high-Z material surrounded by graphite, is comparable to the p-bar targets at CERN and FAIR. In agreement with previous experiments, tantalum has shown its high robustness towards large beam-induced energy deposition densities and the resulting dynamic stresses and temperatures. None of the graphite materials in this work exhibited catastrophic failure. All samples were able to constrict the tantalum cores, ensuring proper operation with respect to p-bar production. But, it has to be assumed that in operational conditions with energy deposition densities beyond $4 \, \text{kJ} \cdot \text{cm}^{-3}$ (e.g., CERN p-bar target), local failure of the surrounding graphite cannot be avoided.

Two observations should be highlighted. While the CFCs presented in this work, SGL Premium PyC and ArianeGroup Sepcarb, have large macroscopic flexural strength in excess of 100 MPa, a change in sample response was observed at energy deposition densities below $1 \, \text{kJ} \cdot \text{cm}^{-3}$. The degradation of the frequency response, according to fast Fourier and continuous wavelet transformation, leads to the assumption that the low-strength graphite matrix (tensile strength of 17 MPa in ArianeGroup Sepcarb) failed locally in those materials. Due to the additional reinforcement of ArianeGroup Sepcarb, which bridges the fiber reinforcement planes, failure in this material occurs at higher intensities than in SGL Premium PyC, which has no additional reinforcement.

The macroscopic response of POCO FOAM, having the lowest flexural strength of the investigated materials, shows strictly linear behaviour with increasing pulse intensity. The dynamic response degraded considerably at pulse intensities beyond 1.2×10^{12} ppp, while the response between 1 and 6×10^{11} ppp is almost constant. This is a promising result for the potential usage of low-strength, low-density graphitic foams as potential energy "diluter" in high-power beam dumps.

Data Availability

The experimental data used to support the findings of this study are available from the corresponding author upon request.

Conflicts of Interest

The authors declare that there are no conflicts of interest regarding the publication of this paper.

Acknowledgments

References

[1] O. S. Brüning, J. Poole, P. Collier et al., *LHC Design Report*, CERN, Geneva, Switzerland, 2004.

[2] H. Gutbrod, "FAIR baseline technical report," *Accelerator and Scientific Infrastructure*, Vol. 2, GSI Helmholtzzentrum, Darmstadt, Germany, 2006.

[3] A. Prosvetov, G. Hamaoui, N. Horny et al., "Degradation of thermal transport properties in fine-grained isotropic graphite exposed to swift heavy ion beams," *Acta Materialia*, vol. 184, pp. 187–198, 2020.

[4] S. Fernandes, F. Pellemoine, M. Tomut et al., "In-situ electric resistance measurements and annealing effects of graphite exposed to swift heavy ions," *Nuclear Instruments and Methods in Physics Research Section B: Beam Interactions with Materials and Atoms*, vol. 314, pp. 125–129, 2013.

[5] C. Hubert, K. O. Voss, M. Bender et al., "Swift heavy ion-induced radiation damage in isotropic graphite studied by micro-indentation and in-situ electrical resistivity," *Nuclear Instruments and Methods in Physics Research Section B: Beam Interactions with Materials and Atoms*, vol. 365, pp. 509–514, 2015.

[6] F. Pellemoine, M. Avilov, M. Bender et al., "Study on structural recovery of graphite irradiated with swift heavy ions at high temperature," *Nuclear Instruments and Methods in Physics Research Section B: Beam Interactions with Materials and Atoms*, vol. 365, pp. 522–524, 2015.

[7] K. Kupka, A. A. Leino, W. Ren et al., "Graphitization of amorphous carbon by swift heavy ion impacts: molecular dynamics simulation," *Diamond and Related Materials*, vol. 83, pp. 134–140, 2018.

[8] M. Tomut, B. Achenbach, K. H. Behr, W. Ensinger et al., *Experimental Investigations on Heavy-Ion Induced Radiation Damage of Graphite for the Super-FRS Target and Beam Catchers*, vol. 69, GSI Scientific Report, Darmstadt, Germany, 2008 http://repository.gsi.de/record/53524.

[9] A. Bertarelli, "Beam-induced damage mechanisms and their calculation," in *Proceedings of the 2014 Joint International Accelerator School: Beam Loss and Accelerator Protection*, Newport Beach, CA, USA, November 2016.

[10] I. Manika, J. Maniks, R. Zabels et al., "Nanoindentation and Raman spectroscopic study of graphite irradiated with Swift238U ions," *Fullerenes, Nanotubes, and Carbon Nanostructures*, vol. 20, no. 4–7, pp. 548–552, 2012.

[11] G. Gobbi, A. Bertarelli, F. Carra, J. Guardia-Valenzuela, and S. Redaelli, "Novel LHC collimator materials: high-energy hadron beam impact tests and nondestructive postirradiation examination," *Mechanics of Advanced Materials and Structures*, vol. 27, no. 17, pp. 1518–1530, 2019.

[12] M. Bergeret, F.-X. Nuiry, M. Calviani et al., "Full scale proton beam impact testing of new cern collimators and validation of a numerical approach for future operation," 2019.

[13] I. Efthymiopoulos, C. Hessler, H. Gaillard et al., "HiRadMat: a new irradiation facility for material testing at CERN," in *Proceedings of the 2nd International Particle Accelerator Conference*, San Sebastian, Spain, November 2011.

[14] F. Harden, A. Bouvard, N. Charitonidis, and Y. Kadi, "HiRadMat: a facility beyond the realms of materials testing," in *Proceedings of the 10th International Particle Accelerator Conference, IPAC2019*, Melbourne Australia, November 2019.

[15] T. T. Böhlen, F. Cerutti, M. P. W. Chin et al., "The FLUKA code: developments and challenges for high energy and medical applications," *Nuclear Data Sheets*, vol. 120, pp. 211–214, 2014.

[16] C. Garion, "Mechanical properties for reliability analysis of structures in glassy carbon," *World Journal of Mechanics*, vol. 4, no. 3, pp. 79–89, 2014.

[17] https://www.hbm.com/en/3443/xy-t-rosettes-with-measuring-grids-for-analyzing-biaxial-stress/.

[18] https://www.polytec.com/eu/vibrometry/products/special-application-vibrometers/rsv-150-remote-sensing-vibrometer/.

[19] https://www.schott.com/advanced_optics/english/products/optical-materials/special-materials/radiation-shielding-glasses/index.html.

[20] C. T. Martin, A. Perillo-Marcone, M. Calviani, L. Gentini, M. Butcher, and J.-L. Muñoz-Cobo, "Experiment exposing refractory metals to impacts of 440 GeV/c proton beams for the future design of the CERN antiproton production target: experiment design and online results," *Physical Review Accelerators and Beams*, vol. 22, no. 1, 2019.

[21] M. Pasquali, A. Bertarelli, C. Accettura et al., "Dynamic response of advanced materials impacted by particle beams: the multimat experiment," *Journal of Dynamic Behavior of Materials*, vol. 5, no. 3, pp. 266–295, 2019.

[22] M. Portelli, A. Bertarelli, F. Carra, M. Pasquali, N. Sammut, and P. Mollicone, "Numerical and experimental benchmarking of the dynamic response of SiC and TZM specimens in the MultiMat experiment," *Mechanics of Materials*, vol. 138, Article ID 103169, 2019.

[23] L. Peroni, M. Scapin, F. Carra, and N. Mariani, "Investigation of dynamic fracture behavior of graphite," *Key Engineering Materials*, vol. 569-570, pp. 103–110, 2013.

[24] https://www.sglcarbon.com/pdf/SGL-Datasheet-SIGRAFINE-R6650-EN.pdf.

[25] http://repository.gsi.de/record/54552 Technical Design Report on the Super-FRS.

[26] https://www.entegris.com/content/dam/shared-product-assets/specialty-shared/datasheet-semiconductor-graphite-7057.pdf.

[27] https://www.sglcarbon.com/pdf/SGL-Datasheet-SIGRABOND-Premium-EN.pdf.

[28] F. X. Nuiry, M. Calviani, M. Bergeret et al., "3D carbon/carbon composites for beam intercepting devices at CERN," *Material Design & Processing Communications*, vol. 1, no. 1, p. e33, 2019.

[29] F. Nuiry and A. Marcone, "Material testing for injection and transfer line absorbers," in *Proceedings of the 5th Joint HiLumi LHC-LARP Annual Meeting*, Geneva, Switzerland, October 2015.

[30] https://www.sglcarbon.com/pdf/SGL-Datasheet-SIGRAFLEX-for-semiconductor-and-LED-industry.pdf.

[31] https://poco.entegris.com/content/en/home/products/premium-graphite/thermal-management-materials/pocofoam.html.

[32] A. Lechner, W. Bartmann, F. Burkart et al., "Dilution requirements for the FCC-hh dump," in *FCC Week*CERN, Amsterdam, Netherland, 2018, https://indico.cern.ch/event/656491/contributions/2947272/attachments/1631698/2601617/2018_12_04_fccdump.pdf.

[33] C. L. Torregrosa Martin, M. Calviani, N. Solieri et al., "First prototypes of the new design of the CERN's antiproton production target," *Material Design & Processing Communications*, vol. 1, no. 2, p. e38, 2019.

[34] C. Torregrosa Martin, M. Calviani, A. Perillo-Marcone et al., "Scaled prototype of a tantalum target embedded in expanded graphite for antiproton production: design, manufacturing, and testing under proton beam impacts," *Physical Review Accelerators and Beams*, vol. 21, no. 7, 2018.

[35] J. Habainy, Y. Lee, K. B. Surreddi et al., "Study of heavy ion beam induced damage in tungsten for high power target applications," *Nuclear Instruments and Methods in Physics Research Section B: Beam Interactions with Materials and Atoms*, vol. 439, pp. 7–16, 2019.

[36] P. Welch, "The use of fast Fourier transform for the estimation of power spectra: a method based on time averaging over short, modified periodograms," *IEEE Transactions on Audio and Electroacoustics*, vol. 15, no. 2, pp. 70–73, 1967.

[37] G. Lee, R. Gommers, F. Waselewski, K. Wohlfahrt, and A. O'Leary, "PyWavelets: a Python package for wavelet analysis," *Journal of Open Source Software*, vol. 4, no. 36, p. 1237, 2019.

[38] I. V. Savchenko and S. V. Stankus, "Thermal conductivity and thermal diffusivity of tantalum in the temperature range from 293 to 1800 K," *Thermophysics and Aeromechanics*, vol. 15, no. 4, pp. 679–682, 2008.

[39] S.-Y. Lin, "Coupled vibration and natural frequency analysis of isotropic cylinders or disks of finite dimensions," *Journal of Sound and Vibration*, vol. 185, no. 2, pp. 193–199, 1995.

[40] A. Mohammadimehr, İ. Solmus, B. Ozyer, and D. A. S. Rees, "Determination of physical properties and thermal conductivity of graphite foam with image analysis," *International Journal of Thermophysics*, vol. 41, no. 4, 2020.

[41] D. Calvo, S. Coli, G. Giraudo, R. Wheadon, and L. Zotti, "Thermal performance of carbon foams used as heat sink for the pixel MVD PANDA," *Journal of Instrumentation*, vol. 6, no. 12, Article ID C12015, 2011.